

2

# NAVAL POSTGRADUATE SCHOOL

## Monterey, California

AD-A206 476



# THESIS

THE EFFECT OF HEAT INPUT AND COMPOSITION  
ON WELD METAL MICROSTRUCTURES IN  
THIN SECTION HY-130 GMAW WELDMENTS

by

Dean M. Pedersen  
December 1988

Thesis Advisor:  
Co-advisor:

Saeed Saboury  
J. M. B. Losz

Approved for public release; distribution is unlimited.

DTIC  
ELECTE  
APR 11 1989  
S D  
C S H

UNCLASSIFIED

SECURITY CLASSIFICATION OF THIS PAGE



## REPORT DOCUMENTATION PAGE

1a REPORT SECURITY CLASSIFICATION <b>UNCLASSIFIED</b>		1b RESTRICTIVE MARKINGS	
2a SECURITY CLASSIFICATION AUTHORITY		3. DISTRIBUTION/AVAILABILITY OF REPORT	
3b DECLASSIFICATION/DOWNGRADING SCHEDULE		Approved for public release; distribution is unlimited.	
4 PERFORMING ORGANIZATION REPORT NUMBER(S)		5 MONITORING ORGANIZATION REPORT NUMBER(S)	
5a NAME OF PERFORMING ORGANIZATION Naval Postgraduate School	6b OFFICE SYMBOL (If applicable) 69	7a NAME OF MONITORING ORGANIZATION Naval Postgraduate School	
6c ADDRESS (City, State and ZIP Code) Monterey, California 93943-5000		7b ADDRESS (City, State, and ZIP Code) Monterey, California 93943-5000	
8a NAME OF FUNDING SPONSORING ORGANIZATION	8b OFFICE SYMBOL (If applicable)	9 PROCUREMENT INSTRUMENT IDENTIFICATION NUMBER	
8c ADDRESS (City, State and ZIP Code)		10 SOURCE OF FUNDING NUMBERS	
		PROGRAM ELEMENT NO	PROJECT NO
		TASK NO	WORK UNIT ACCESION NO
11 TITLE (Include Security Classification) The Effect of Heat Input and Composition on Weld Metal Microstructures on Thin Section HY-130 GMAW Weldments.			
12 PERSONAL AUTHOR(S) Pedersen, Dean M.			
13a TYPE OF REPORT Master's Thesis	13b TIME COVERED FROM _____ TO _____	14 DATE OF REPORT (Year, Month, Day) December 1988	15 PAGE COUNT 94
16 SUPPLEMENTARY NOTATION The views expressed in this thesis are those of the author and do not reflect the official policy or position of the Department of Defense or the U. S. Government.			
17 COSAT CODES		18 SUBJECT TERMS (Continue on reverse if necessary and identify by block number) HY-130, GMAW, Weld Metal Microstructure	
FIELD	GROUP	SUB-GROUP	
19 ABSTRACT (Continue on reverse if necessary and identify by block number) Thin section HY-130 is being considered by the U. S. Navy for use in decks and foundations in the SSN-21 design as a weight saving measure. Optimum welding procedures for thin section HY-130 do not currently exist, but they are being developed by David Taylor Naval Ship Research and Development Center (DTNSRDC). In this study, performed in conjunction with DTNSRDC, the effect of heat input and electrode composition on the weld metal microstructures and mechanical properties of four 12.7 mm thick HY-130 steel weldments produced by the GMAW process are reported. Microstructures were fully characterized by light and electron microscopy. Mechanical property results provided by DTNSRDC were correlated with the microstructure. The lower heat input produced microstructural refinement and a more uniform hardness. The higher carbon content electrode lowered the Ms temperature and stabilized the austenite. A microduplex structure of lath martensite and			
20 DISTRIBUTION AVAILABILITY OF ABSTRACT <input checked="" type="checkbox"/> UNCLASSIFIED/UNLIMITED <input type="checkbox"/> SAVE AS RPT <input type="checkbox"/> DISTR. BY USERS		21 ABSTRACT SECURITY CLASSIFICATION <b>UNCLASSIFIED</b>	
22a NAME OF RESPONSIBLE INDIVIDUAL Saeed Saboury		22b TELEPHONE (Include Area Code) (408) 372-5932	22c OFFICE SYMBOL 69Sb

DD FORM 1473, 24 MAR

83 EDITION MAY BE USED UNTIL EXHAUSTED  
ALL OTHER EDITIONS ARE OBSOLETE

SECURITY CLASSIFICATION OF THIS PAGE

U. S. Government Printing Office 1988-606-243

UNCLASSIFIED

#19 - Continued

thin film interlath retained austenite produced a good combination of strength and toughness.

C

Accession For	
NTIS GRAAI	<input checked="" type="checkbox"/>
DTIC ZAB	<input type="checkbox"/>
Unannounced	<input type="checkbox"/>
Justification	
By _____	
Distribution/	
Availability Codes	
Dist	Avail and/or Special
A-1	

APPROVED FOR PUBLIC RELEASE: DISTRIBUTION IS UNLIMITED.

THE EFFECT OF HEAT INPUT AND COMPOSITION  
ON WELD METAL MICROSTRUCTURES IN  
THIN SECTION HY-130 GMAW WELDMENTS

BY

Dean M. Pedersen  
Lieutenant, United States Navy  
B. S. Chemical Engineering, Purdue University, 1973

Submitted in partial fulfillment of the  
requirements for the degree of

MASTER OF SCIENCE IN MECHANICAL ENGINEERING

from the

NAVAL POSTGRADUATE SCHOOL  
December 1981

Approved:

*Dean M. Pedersen*  
Dean M. Pedersen

Approved by:

*Seed Savory*  
Seed Savory, Thesis Advisor

*J. M. B. Losz*  
J. M. B. Losz, Thesis Co-Advisor

*D. J. Healey*  
D. J. Healey, Chairman

Department of Mechanical Engineering

*Gordon E. Schacher*  
Gordon E. Schacher  
Dean of Science and Engineering

## ABSTRACT

Thin section HY-130 is being considered by the U. S. Navy for use in decks and foundations in the SSN-21 design as a weight saving measure. Optimum welding procedures for thin section HY-130 do not currently exist, but they are being developed by David Taylor Naval Ship Research and Development Center (DTNSRDC). In this study, performed in conjunction with DTNSRDC, the effect of heat input and electrode composition on the weld metal microstructures and mechanical properties of four 12.7 mm thick HY-130 steel weldments produced by the GMAW process are reported. Microstructures were fully characterized by light and electron microscopy. Mechanical property results provided by DTNSRDC were correlated with the microstructure. The lower heat input produced microstructural refinement and a more uniform hardness. The higher carbon content electrode lowered the  $M_e$  temperature and stabilized the austenite. A microduplex structure of lath martensite and thin film interlath retained austenite produced a good combination of strength and toughness.

## TABLE OF CONTENTS

I.	INTRODUCTION.....	1
II.	BACKGROUND.....	4
	A. MICROCONSTITUENTS.....	5
	B. MECHANICAL PROPERTIES.....	9
	C. EFFECT OF HEAT INPUT.....	13
	D. EFFECT OF COMPOSITION.....	15
	E. HY-130 MICROSTRUCTURES OBSERVED.....	17
III.	EXPERIMENTAL PROCEDURE.....	19
	A. MATERIAL.....	19
	B. MACROSAMPLE PREPARATION.....	19
	C. MECHANICAL PROPERTIES.....	24
	D. MICROSTRUCTURAL CHARACTERIZATION.....	25
IV.	RESULTS.....	28
	A. MECHANICAL TESTING.....	28
	B. MICROSTRUCTURAL CHARACTERIZATION.....	32
V.	DISCUSSION.....	42
	A. MICROSTRUCTURE.....	42
	B. EFFECT OF HEAT INPUT.....	45
	C. EFFECT OF COMPOSITION.....	47
VI.	CONCLUSIONS.....	50
VII.	RECOMMENDATIONS.....	51
	APPENDIX.....	52
	LIST OF REFERENCES.....	84
	INITIAL DISTRIBUTION LIST.....	87

#### ACKNOWLEDGEMENTS

I wish to express my appreciation to my thesis advisors, Dr. J. Mauro Losz and Dr. Saeed Saboury for their guidance and assistance in completing this work. A special thanks to Dr. Losz for his many hours of TEM analysis on my behalf and for sharing his expertise in the areas of TEM and micrographic analysis.

I would also like to express my sincere thanks to my wife, Pam, for all her help in keeping our house a home through the turmoil caused by my work. Finally, I dedicate this work to my children, David and Donna.

## I. INTRODUCTION

HY-130 is a 5Ni-Cr-Mo-V steel, required to contain less than 0.12 wt% carbon and exhibit a minimum yield strength of 130 ksi (896 MPa) [Ref. 1]. This hardenable steel was developed by the U. S. Navy for naval applications where high strength along with good toughness and weldability are the major requirements. The combination of high strength with good resistance to brittle fracture is based on the development of a tempered martensite-bainite microstructure produced after a quench and temper heat treatment.

HY-130 can be welded by a variety of processes, including the multipass Gas Metal Arc Welding (GMAW) process. It is welded with a filler metal slightly different from the base metal, the composition of which is designed to produce an as-deposited weld metal strength and toughness that closely resembles the heat treated strength and toughness of the base metal [Ref. 2]. No post weld heat treatment is required to produce the specified mechanical properties across the weld zone [Ref. 1].

A clean steel making process, possibly with vacuum degassing, is critical to minimize the introduction of impurities, thus retaining the desired mechanical properties. Welding procedures for HY-130 are more stringent than for HY-80, but a welding system suitable for shipyard fabrication is currently available for thick plate HY-130. Weldment

problems for HY-130 are very different than for HY-80: HY-80 is prone to heat affected zone (HAZ) cracking while HY-130 is much more likely to exhibit weld metal cracking and porosity. Both steels possess good resistance to stress corrosion cracking and adequate ductility for either cold or hot forming. [Ref. 1]

Thin section (less than 19 mm thick) HY-130 steel is being considered for nonpressure hull applications in the SSN-21 submarine design. A design analysis performed by Electric Boat [Ref. 3] showed that significant weight savings could be achieved by replacing HY-100 with HY-130 in the fabrication of decks and foundations. David Taylor Naval Ship Research and Development Center (DTNSRDC) is presently developing welding procedures for HY-130 in thicknesses of 6.4 to 19 mm. Welding variables such as preheat, heat input, joint design, welding process, electrode composition, flux, etc. are being examined to produce strength and toughness levels similar to the base metal across the weld region and the heat affected zone [Ref. 4].

The present research was initiated at the Naval Postgraduate School based on a request by DTNSRDC for additional information on the microstructure of GMAW weldments previously fabricated as part of the Center's analysis of thin section HY-130. This study investigates the effects of heat input and electrode composition on the microstructure and mechanical properties of four GMAW

weldments in 12.7 mm thick HY-130 plates. The weld metal microstructures were characterized by light and electron microscopy techniques and mechanical properties were assessed using Charpy V-Notch (CVN), tensile and hardness tests.

## II. BACKGROUND

The strength and hardness of welds is generally high due to alloying elements working in combination with rapid cooling rates to promote the formation of low temperature transformation products, primarily bainite and martensite. On the other hand, the impact and toughness properties of steel welds are not usually high because of the inhomogeneity of the weld metal microstructure resulting from a relatively coarse columnar solidification structure and due to segregation. [Ref. 5]

The attainment of both strength and toughness in as-deposited HY-130 GMAW weldments requires a delicate balance between composition and cooling rate to produce the required microstructure in a multipass weld. The location of greatest concern within the weld metal is generally the final weld pass. It is expected to exhibit the highest hardness and the least refined microstructure due to the lack of thermal cycling from subsequent weld passes [Ref. 2]. Various microconstituents observed in GMAW weldments, the relationship between microstructure and mechanical properties, and the roles of cooling rate and composition in forming these microstructures are discussed in this chapter.

## A. MICROCONSTITUENTS

The microstructure of the fusion zone in weld metals is dependent upon the welding process, bead size, heat input, electrode composition, preheat temperature and base metal thickness [Ref. 2]. The thermal effects of the welding cycle can cause multi-constituent microstructures to be observed on a very fine scale in the fusion zone of steel welds, particularly in multipass welding. The microconstituents most commonly observed in the fusion zone of weld metals include lath and twinned martensite, tempered and autotempered martensite, retained austenite, martensite-austenite, bainite, acicular ferrite and non-metallic inclusions.

### 1. Martensite

Martensite is a low temperature transformation product and as such it requires a very fast cooling rate to form. Martensite begins to form at the martensite start ( $M_s$ ) temperature and the transformation is completed at the martensite finish ( $M_f$ ) temperature. Martensite nucleates and grows by a diffusionless shear mechanism so it maintains the same composition as the parent austenite. "Surfaces," such as grain boundaries or inclusions, are not particularly good nucleation sites for martensite; it generally prefers to nucleate within the prior austenite grains on dislocations, or groups of dislocations, so it can use the strain energy of the dislocation as an aid to nucleation. Lath martensite

with a very high dislocation density is typically observed in low carbon steel weld metals; it generally grows in packets on {111} habit planes. The high hardness of lath martensite is due to its high dislocation density along with the carbon in solid solution. [Ref. 5]

Twinned martensite contains at least 0.5 wt% C and is generally found only when the carbon content is greater than 0.15 wt% [Refs. 2 and 6]. It may form in HY-130 weldments due to carbon segregation [Ref. 2].

## **2. Tempered and Autotempered Martensite**

Martensite is not an equilibrium microstructure so it can be tempered by heating after formation. Tempered martensite is softer and more ductile than untempered martensite due to the precipitation of cementite from the previously untempered martensite. Tempered martensite may be observed in multipass weld metals due to thermal cycling from subsequent weld passes [Ref. 7]. Autotempered martensite is a slightly different morphology that may be seen in higher heat input welds in which lath martensite forms at a temperature high enough to allow some tempering during further cooling without additional heat being supplied.

## **3. Retained Austenite**

As the martensite laths form during cooling after welding, they surround and isolate small islands of austenite. The austenite requires more space to transform to martensite so the existing martensite must crack or the

austenite is forced to remain untransformed in the microstructure as retained austenite [Ref. 7]. In weld metals with high cooling rates, retained austenite may exist in very thin regions between the martensite laths [Ref. 5]. Interlath films of retained austenite are usually detected only by transmission electron microscopy (TEM) [Ref. 8].

#### **4. Martensite-Austenite**

Martensite-austenite is a microconstituent consisting of regions of high carbon (about 0.5 wt% C) martensite surrounded by retained austenite. As austenite transforms to bainitic ferrite by nucleation and growth, the remaining austenite is continually enriched in carbon. If the carbon partitioned to the austenite does not become locally concentrated sufficiently to cause nucleation of cementite, martensite-austenite is formed. Microtwins are often observed within the martensite-austenite constituent. Higher alloy contents provide greater austenite stability, suppress cementite precipitation from carbon enriched austenite, and increase the amount of martensite-austenite formed. [Ref. 9]

#### **5. Lower Bainite**

At temperatures just above the  $M_a$  temperature, lower bainite laths may nucleate and grow if carbon diffusion at the austenite grain boundaries is sufficient. The growth of lower bainite is an interface controlled reaction that relies on very short range diffusion of carbon to form carbides with an orientation relationship to the ferrite, concurrent with a

thickening and lengthening of the plates. At the low growth temperature of lower bainite, carbon diffusion is so slow that the ferrite plates thicken easier by precipitation of cementite at the interface. Thus, excess carbon is removed from the austenite and the interface between the austenite and the growing bainite laths advances [Ref. 5].

#### 6. Acicular Ferrite

Generally considered to be the most desirable microconstituent in weld metal, acicular ferrite consists of a series of very fine interlocking ferrite laths (typical sizes are 0.1-3.0  $\mu$ ) that generally form within the prior austenite grains [Ref. 10]. Acicular ferrite is known to enhance both toughness and strength in weld metals. The laths are separated by high-angle grain boundaries and often contain complex second phases at the boundary, such as retained austenite, martensite and carbides. The nucleation of acicular ferrite laths is most favorable at austenite grain boundaries, although non-metallic inclusions have been identified as the primary nucleation sites [Ref. 11]. Without potent nucleation sites for ferrite (a weld metal oxygen content <0.01 wt% for instance), the formation of acicular ferrite may be completely suppressed [Refs. 12 and 13].

#### 7. Non-Metallic Inclusions

Indigenous non-metallic inclusions, primarily glassy, spherical silicon and manganese oxides, form as a result of

deoxidation reactions in liquid weld metal as it cools [Ref. 12]. When using a consumable electrode, as in GMAW, oxidation of the alloying elements takes place in the droplets as they form at the electrode tip so there is very little reaction in the weld pool [Ref. 14].

Inclusions can exist with diameters up to  $10 \mu$ , although weld metal inclusions are normally less than  $1 \mu$  in diameter; volume fractions as high as 1% have been observed [Ref. 14]. Particle coarsening is primarily due to coalescence of smaller particles into larger ones. The average diameter generally increases with aluminum content (because aluminum is the strongest oxide former commonly used for deoxidation of steel) and with heat input (due to an extended weld pool retention time) [Ref. 12].

Nucleation of acicular ferrite on inclusions is always more favorable than homogeneous nucleation, but less favorable than nucleation on austenite grain boundaries, regardless of the inclusion size. It appears that inclusions with diameters from  $0.4-1.0 \mu$  are the most potent nucleation sites for acicular ferrite [Ref. 12]. Smaller inclusions may pin the austenite grain boundaries, thus restricting grain size and providing good nucleation sites for polygonal ferrite [Ref. 10].

## B. MECHANICAL PROPERTIES

The achievement of the specified strength and toughness properties for HY-130 base plate requires a tempered

microstructure of 60 to 75% martensite as a minimum, with the remainder as fine lower bainite [Ref. 15]. Refinement of the weld metal microstructure may yield increases in both strength and toughness which are generally not simultaneously possible. A refined structure (i.e., a fine grained bainitic or ferritic structure) generally promotes ductile fracture and gives the best resistance to environmental embrittlement in HY-130 weldments [Ref. 16]. Thus by lowering the  $M_a$  temperature, nucleation sites for bainite laths are increased and packet widths are refined producing a lower ductile to brittle transition temperature and improved toughness.

Conner et al. [Ref. 17] conducted an extensive study of the mechanical properties of HY-130 GMAW weldments using several different electrodes, heat inputs, preheat/interpass temperatures and plate thicknesses including 12.7 mm thin sections. They reported a good combination of strength and toughness for a 0.08 wt% carbon electrode using a heat input of 1.46 kJ/mm and a preheat/interpass temperature of 65°C.

Glover et al. [Ref. 6], working with C/Mn steel weldments, observed a higher fracture toughness associated with a fine acicular ferrite structure and a low inclusion content, while martensite, martensite-austenite and coarse upper bainite had a deleterious effect on weld metal toughness. Sarikaya et al. [Ref. 18] associated inferior toughness with a high density of large oxide inclusions. The problem of poor impact toughness in welds may be compounded

by the formation of martensite-austenite or carbides on ferrite boundaries where they may act as efficient crack nucleation sites [Ref. 6]. Biss and Cryderman [Ref. 9] report that martensite-austenite can cause poor impact properties and lower yield strength in low carbon steels.

A microduplex structure of dislocated-autotempered lath martensite and thin film interlath retained martensite produced good combinations of strength and toughness for Fe/Cr/C base steels [Ref. 18]. Significant increases in toughness in particular have been attributed to these martensite/stable retained austenite structures.

Tempering introduced by thermal cycling in multipass weldments may produce a significant increase in impact energy along with an improvement in yield strength due to the precipitation of very fine, intralath carbides [Ref. 18]. Unfortunately, tempering may also cause tempered martensite embrittlement due to thermally unstable retained austenite [Refs. 8 and 18]. Embrittlement often observed near 260°C is due to the precipitation of film-like carbides on prior austenite grain boundaries and sub-boundaries [Ref. 19]. Segregation of alloying elements, especially manganese and chromium, to prior austenite grain boundaries can compound problems with temper embrittlement. Silicon can be added to postpone the tempering of martensite during thermal cycling [Ref. 19].

Hydrogen embrittlement and stress corrosion cracking (SCC) are also strong functions of microstructure. Chen et al. [Ref. 16] report the microstructures most susceptible to SCC are transformation twinned martensite and coarse laths of bainitic ferrite, while fine lath martensite is the most resistant. HY-130 is particularly susceptible to hydrogen damage as a result of the high solubility of hydrogen in nickel alloyed steels, thus the hydrogen content should be kept below 2 ppm [Ref. 15]. Ritchie et al. [Ref. 20] report that retained austenite reduces SCC crack velocity by lowering the susceptibility to hydrogen embrittlement. In sharp contrast, Kim et al. [Ref. 21] conclude, in a study of 5.5 Ni steel, that unstable interlath retained austenite may increase susceptibility to hydrogen embrittlement. HY-130 plates one inch thick have been welded with a preheat and interpass temperature of 66°C with no signs of hydrogen-assisted weld metal cracks [Ref. 17]. Satisfactory resistance to hydrogen related problems has not been demonstrated for non-preheated HY-130 weldments.

Multipass welding provides thermal cycling for all weld passes except the final pass. Challenger et al. [Ref. 2] postulate that softening occurring during multipass welding is due to either carbon segregation or precipitation of carbides on a scale too fine to observe with standard TEM techniques.

### C. EFFECT OF HEAT INPUT

The transformation kinetics and the mechanical properties of weld metal are strongly influenced by the cooling rate. Increasing the cooling rate is an ideal mechanism for microstructural refinement, but such an increase may also result in delayed weld metal cracking or an undesirable microstructure [Ref. 17]. The cooling rate from 800 to 500°C following welding is considered indicative of the properties to be anticipated. The Rosenthal equation [Ref. 22] shows that cooling rate is inversely proportional to heat input with the same metal, welding velocity and preheat so these terms can be used interchangeably (i.e., an increase in cooling rate occurs due to a decrease in heat input).

Higher cooling rates are generally associated with low temperature transformation products which produce increases in strength, but decreases in toughness [Ref. 22]. At slow cooling rates in C/Mn steel weldments, Glover et al. [Ref. 6] show, via a schematic CCT diagram, that austenite should transform to coarse polygonal ferrite with regions of pearlite, while intermediate cooling rates cause coarse ferrite to form along austenite grain boundaries initially with acicular ferrite forming inside the prior austenite grains as the transformation temperature decreases. At a very fast cooling rate (heat input of 0.74 kJ/mm), austenite should transform to an upper bainitic structure with no proeutectoid ferrite at the prior austenite grain boundaries;

a lower bainite start temperature yields colonies of finer bainite.

Argon base shielding gases typically produce a central region of deep penetration known as the papilla [Ref. 23]. Deep papillae exhibit high cooling rates causing low toughness and low ductility in this region, thus reducing the benefits of multipass welding [Ref. 2]. High heat inputs are generally required for depositing large weld beads, thus increase the rate of welding. Porosity is generally low in low heat input weldments because the weld pool remains shallow and allows most of the gas bubbles to escape before the pool solidifies [Ref. 17].

Farrar and Harrison [Ref. 10] report that high cooling rates coupled with basic hardenability produce a true martensitic transformation in the weld metal of steels containing manganese and nickel. They conclude that the major influence of cooling rate is in determining the degree of supercooling prior to the transformation, hence it needs to be balanced to the basic hardenability of the austenite matrix.

Strength generally decreases slightly as the preheat temperature or the heat input is increased. The yield strength decrease for a given increase in heat input is larger than the decrease for a variation in preheat/interpass temperature [Ref. 23].

A minimum cooling rate of 16.7°C/sec is specified for HY-130 weldments [Ref. 24]. This minimum cooling rate requirement limits the maximum allowable preheat temperature, but necessarily so because slower cooling rates will result in weld metal with unacceptably low yield strength. Heat inputs of 1.38 to 1.57 kJ/mm with preheat and interpass temperatures in the range 52 to 66°C have proven optimal for achieving mechanical properties in the target area for HY-130 welds in plate thicknesses of 9.5 to 16 mm [Refs. 17 and 23].

#### D. EFFECT OF COMPOSITION

Weld metals are essentially subjected to continuous cooling during solidification, so the resultant microstructures should be predictable from CCT diagrams. Unfortunately, these diagrams are not readily available for weld metals and would actually be extremely difficult to develop based on the composition and cooling rate variation just within a single weld pass.

Although individual CCT diagrams for weld metals are generally not available, the influence of certain features of welding such as cooling rate and composition on the formation of microconstituents can be predicted. Austenite stabilizers (C, N, Mn, Ni, Cu) push transformation to longer times and enhance the formation of low temperature products such as bainite and martensite. Microalloying elements such as niobium, titanium and vanadium may cause grain hardening and

reduced toughness due to precipitation reactions during thermal cycling in multipass welding. [Ref. 5]

Addition of molybdenum seems to delay the polygonal ferrite reaction, favor the formation of bainitic structures and increase the amount of acicular ferrite formed [Ref. 10]. Molybdenum may also limit or postpone tempered martensite embrittlement by providing temper resistance [Ref. 18].

Excessive amounts of carbon, sulfur, phosphorus, hydrogen, oxygen and nitrogen can cause weld metal cracking in HY-130 welds [Ref. 24]. On the other hand, weld metal compositions with high oxygen contents generally exhibit higher inclusion densities which in turn promote the formation of acicular ferrite, a microstructure important for good weld toughness [Ref. 22]. Abson and Dolby [Ref. 13] show the level of oxygen significantly influences the position of the acicular ferrite phase field in a weld metal CCT diagram. They report the formation of acicular ferrite is most favorable with a weld metal oxygen content of 0.03 wt%. From their analyses, Bhatti et al. [Ref. 25] conclude the formation of acicular ferrite is favored by aluminum rich rather than manganese rich inclusions.

Carbon has more control of the microstructure in steel weld metal than any other element; it is responsible for the amounts of lath martensite and carbides formed and exerts a significant influence on the solidification substructure. At a fixed cooling rate, Glover et al. [Ref. 6] report that

lowering the carbon level in untransformed austenite via segregation raises the local  $M_a$  temperature. This also decreases the available carbon supersaturation for carbide nucleation so the formation of martensite-austenite rather than carbides is favored. Challenger et al. [Ref. 2] reported the same effect of carbon content on  $M_a$  temperature in HY-130 weldments. Andrews' empirical product formula [Ref. 26] gives  $M_a$  temperature as a function of composition:

$$M_a (\text{ }^{\circ}\text{C}) = 512 - 453(\%C) - 16.9(\%Ni) + 15(\%Cr) - 9.5(\%Mn) + 217(\%C)^2 - 71.5(\%C)(\%Mn) - 67.6(\%C)(\%Cr).$$

#### E. HY-130 MICROSTRUCTURES OBSERVED

Employing thin foil transmission electron microscopy, Challenger et al. [Ref. 2] observed primarily lath martensite (0.24  $\mu$  average width) with a high dislocation density and large spherical carbides in tempered HY-130 base metal. In HY-130 weld metal with a heat input of 2.05 kJ/mm, they observed fine lath martensite (about 0.2  $\mu$  average width) and wide bainite laths (about 2  $\mu$  average width) with no carbides in the martensite. They also observed the presence of twinned martensite in bainite within HY-130 weld zones due to carbon segregation [Ref. 2].

Structures of martensite, also twinned and autotempered martensite, with small amounts of bainite were seen by Chen et al. [Ref. 16] in a thick section HY-130 weld metal fabricated by the GMAW process with a heat input of 1.8 kJ/mm

and a preheat/interpass temperature of 135-149°C. They observed a mixed bainitic structure with large amounts of broad lath lower bainite, twinned martensite and some rare retained austenite in a similar weld with a heat input of 1.6 kJ/mm and a preheat/interpass temperature of 65-135°C.

### III. EXPERIMENTAL PROCEDURE

#### A. MATERIAL

Four HY-130 steel plates 12.7 mm thick, with the chemical compositions given in Table 1, were welded in the flat position by the GMAW process. The welding joint design for each plate was a single beveled 45 degree V-joint with a 6.4 mm thick backing plate tack welded to the base of each plate. Two different electrode materials were used; their chemical compositions are given in Table 2. As shown in Table 3, two of the specimens (Samples W2 and W6) were welded with electrode Linde 151140 at heat inputs of 0.79 and 1.61 kJ/mm, while the other two specimens (Samples W58 and W60) were welded with electrode LTEC 140005 at the same two heat inputs. The composition of the as-deposited weld metal for each sample is presented in Table 4.

#### B. MACROSAMPLE PREPARATION

A 12.7 mm thick slice perpendicular to the welding direction was cut out of the center of each weldment, ground and polished for macroetching. The samples were then etched in a 2% Nital solution for 10 minutes to reveal the details of each weld pass. Figures 1-4 illustrate the macrostructure for each weldment (all figures appear in the appendix).

TABLE 1  
CHEMICAL COMPOSITION OF HY-130 BASE PLATE (WT%)

Element	Specification	Base Plate
Carbon	0.12 Max	0.09
Manganese	0.60 - 0.90	0.71
Phosphorus	0.010 Max	0.008
Sulfur	0.010 Max	0.003
Silicon	0.20 - 0.35	0.28
Copper	0.25 Max	0.15
Nickel	4.75 - 5.25	4.83
Chromium	0.40 - 0.70	0.54
Molybdenum	0.30 - 0.65	0.41
Vanadium	0.05 - 0.10	0.08
Titanium	0.02 Max	0.005

TABLE 2  
CHEMICAL COMPOSITION OF HY-130 ELECTRODE WIRES (WT%)

Element	Linde 151140	LTEC 140005
Carbon	0.099	0.076
Manganese	1.59	1.55
Phosphorus	0.004	0.004
Sulfur	0.008	0.002
Silicon	0.38	0.39
Copper	0.054	0.031
Nickel	2.67	2.47
Chromium	0.69	0.73
Molybdenum	0.95	0.80
Vanadium	0.003	0.003
Titanium	0.012	0.016
Zirconium	0.004	0.002
Aluminum	0.006	0.005
Oxygen	0.056	0.022
Nitrogen	0.004	0.008

TABLE 3  
WELDING CONDITIONS EMPLOYED

Condition	Sample W2	Sample W6	Sample W58	Sample W60
Electrode Wire (1.14 mm diameter)	Linde 151140	Linde 151140	LTEC 140005	LTEC 140005
Travel Speed (mm/sec)	8.5	4.2	8.5	4.2
Heat Input (kJ/mm)	0.79	1.61	0.79	1.61
Cooling Rate (°C/sec)	38.6	13.0	38.6	13.0
Current (amps)	260	260	260	260
Voltage (Volts)	26	26	26	26
Preheat/Interpass Temperature (°C)	65 - 93	65 - 93	65 - 93	65 - 93
Shielding Gas	M2*	M2*	M2*	M2*

\* 98% argon, 2% oxygen

TABLE 4  
CHEMICAL COMPOSITION OF AS-DEPOSITED WELD METAL (WT%)

Element	W2	W6	W58	W60
Carbon	0.081	0.093	0.067	0.061
Manganese	1.09	1.20	1.44	1.38
Phosphorus	0.002	0.002	0.006	0.001
Sulfur	0.005	0.001	0.001	0.001
Silicon	0.28	0.29	0.39	0.37
Copper	0.087	0.078	0.040	0.041
Nickel	3.62	3.36	2.70	2.72
Chromium	0.60	0.64	0.67	0.71
Molybdenum	0.70	0.79	0.82	0.79
Vanadium	0.045	0.035	0.007	0.010
Titanium	0.005	0.005	0.009	0.007
Zirconium	0.001	0.001	0.004	0.003
Aluminum	0.012	0.013	0.006	0.006
Oxygen	0.021	0.002	0.021	0.025
Nitrogen	0.006	0.008	0.005	0.005

## C. MECHANICAL PROPERTIES

### 1. Hardness Testing

Rockwell C hardness measurements were recorded using a Wilson Rockwell hardness tester with a 150 kg load and a brale indentor. Rockwell hardness values are based on the average of at least three indentations at random locations within each weld pass.

For microhardness measurements, the macrosample slices were cut to remove the backing plate and the remainder of the base metal. A diamond wafering saw was used to cut a slice about 6 mm thick from each sample perpendicular to the weld direction. Each slice was mounted in a cylindrical mold using a fast cure acrylic with the diamond cut side exposed, polished by standard metallographic techniques and etched for 15 seconds in 2% Nital to reveal the weld passes. A line was scribed on each sample as a reference for locating microhardness marks and identifying location (Figures 1-4). A Buehler micromet microhardness tester with a 300g load, a diamond pyramid indentor and a 600X optical system was used to measure the Vickers hardness at 0.2 mm intervals along the four scribe lines.

### 2. Tensile and Impact Testing

Tensile and impact testing for the base plate as well as for the weld metal from each weldment was performed by DTNSRDC. The tensile properties were determined by duplicate tests on longitudinal 8.9 mm diameter specimens taken from

the weld metal region. The specimens and procedures conform to type R-3 of MIL-STD-418C [Ref. 3]. Standard Charpy V-notch (CVN) specimens were used to evaluate the impact toughness of the base plate and the weldments at -17.8°C and 0°C respectively.

#### D. MICROSTRUCTURAL CHARACTERIZATION

##### 1. Optical Microscopy

A Zeiss ICM 405 Photomicroscope was used for optical analysis. The mounted samples used for microhardness testing were repolished and etched for 45 seconds in 2% Nital. Micrographs at 500X and 1000X were taken at the high, low and average hardness points along the scribe lines. In addition, optical micrographs at random locations within the last weld pass were taken at both 500X and 1000X. Oberhoffer's solution [Ref. 27] with the following chemical composition:

- \* FeCl<sub>3</sub> 30g
- \* CuCl<sub>2</sub> 1g
- \* SnCl<sub>2</sub> 0.5g
- \* HCl 50ml
- \* C<sub>2</sub>H<sub>5</sub>OH 500ml
- \* H<sub>2</sub>O 500ml

was used as an etchant for 1 minute and 15 seconds to reveal the cellular-dendritic solidification structure. After repolishing, the grain solidification structures of Samples W58 and W60 were photographed using 2% Nital for 45 seconds as the etchant.

## 2. Scanning Electron Microscopy

The specimens were removed from their acrylic mounts and placed on a tray in the vacuum chamber of a Cambridge Stereo Scan S4-10 Scanning Electron Microscope (SEM). The stage was tilted 10 degrees from horizontal to improve resolution. The microhardness indentations were again used as reference points to take micrographs at approximately 2000X near the points corresponding to the low, average and high hardness for each sample.

## 3. Transmission Electron Microscopy

After the 6 mm slice for microhardness had been removed from a sample using the diamond wafering saw, a second cut was made to produce a slice approximately 0.3 mm thick. This slice was glued to an aluminum block and ground to a thickness of approximately 0.15 mm using 400 and 600 grade silicon carbide paper. Each thinned slice was etched about 15 seconds in 2% Nital to reveal the weld passes and 3 mm diameter disks were mechanically punched from the material of the last weld pass. The last weld pass was selected for TEM examination because it was expected to be the location of the most significant differences in the microstructure between the four samples. The disks were then carefully ground on 600 grade silicon carbide paper to a thickness of approximately 0.08 mm to remove any corrosion layer and to provide a uniform thickness. Final thinning was performed in a Streuers Tenupol electropolishing device with a 10%

perchloric acid - 90% glacial acetic acid solution as electrolyte at an applied voltage of 50 volts and a current of 180 mA and a temperature of 13°C. The foils were examined with a JEOL-100 CX Transmission Electron Microscope operating at 120 KV.

## IV. RESULTS

### A. MECHANICAL TESTING

#### 1. Hardness Testing

Values of Rockwell C hardness for each weld pass in all four samples as identified in Figures 1-4 are listed in Table 5. These hardness measurements generally increase from weld pass #1 to the highest numbered weld pass; this trend is very clear for the higher heat input samples, W6 and W60. The highest hardness corresponds with the highest numbered weld pass, except in the case of Sample W2. The higher Rockwell hardness reading measured in pass #13 of Sample W2 as compared to pass #14 indicates that pass #13 was probably the last pass for this sample, not pass #14 as originally assumed. The hardness of the base metal was nearly identical for all weldments, as anticipated, because they were all fabricated from the same plate. The two welds with the low heat input, Samples W2 and W58, had a similar average hardness, while the high heat input welds both had a lower hardness. The average hardness of Sample W60 was significantly lower than the other three.

Vickers microhardness measurements from the weld crown area down toward the root area for the traverses indicated in Figures 1-4 are illustrated in Figures 5-8. The distance indicated in Figures 5-8 is measured from the starting point S. The traverse paths were selected to

TABLE 5  
ROCKWELL C HARDNESS MEASUREMENTS

Weld Pass Number	W2	W6	W58	W60
1	34.8	31.0	34.7	32.0
2	34.0	32.8	34.7	29.7
3	36.0	31.6	34.5	30.3
4	34.0	32.8	34.0	31.3
5	34.3	33.5	34.0	32.7
6	36.3	34.5	34.0	33.0
7	34.5	34.5	34.3	33.0
8	34.5	37.0	34.7	33.5
9	33.5	---	34.0	---
10	34.3	---	35.3	---
11	34.5	---	35.0	---
12	33.0	---	35.3	---
13	39.0	---	34.0	---
14	33.3	---	34.3	---
15	---	---	37.3	---
Average	34.7	33.4	34.7	31.9

include at least three weld passes, one of which was assumed to be the last pass completed in the welding process. The low, average and high hardness indentations for each sample were recorded and used for microstructural analysis.

Hardness drops of 20 - 60 VHN typically occurred as the traverse went from the heat affected zone of one pass to a previous pass. Point A in Figures 5-8 marks the approximate passage from the heat affected zone of the crown weld pass to one of the previous passes. Points B and C in Figures 5-8 likewise indicate the passage from one heat zone to a previous zone. Point D in Figure 7 is where a fourth drop in hardness was recorded, due primarily to the fact that Sample W58 had more weld passes than any other sample. Sample W58 exhibited the highest average hardness in the highest numbered weld pass followed by W6, W2 and finally W60. An identical order was seen for the complete traverse average hardness. The peak hardness in the highest numbered weld pass was significantly higher than the peak hardness recorded in earlier passes, except for Sample W2.

## **2. Tensile and Impact Testing**

The results of the tensile and impact tests performed by DTNSRDC for the base plate and the weldments are presented in Table 6. Sample W2 exhibited the highest strength and impact toughness; both values exceeded the specifications, although the specification temperature and the experimental temperature for Sample W2 were not the same. Sample W2

TABLE 6  
MECHANICAL PROPERTIES OF BASE PLATE AND WELDMENTS

Identification	0.2% Offset YS (MPa)	UTS (MPa)	Elongation (%)	Reduction in Area (%)	CVN(J)	
					0°C	-18°C
HY-130 Plate Specifications (MIL-S-24371A)	896	---	14	---	---	81.4
Base Plate	959	1034	23	68.5	---	103.1
W-2	982.5	1041	20	62.5	93.6	---
W-6	923.9	965	24	66.0	79.6	---
W-58	944.6	1082	21	62.5	74.1	---
W-60	789.5	1069	18	64.0	78.2	---

showed a yield strength 2.5% higher than the base plate, but an impact energy at least 9% less. The other three samples had low impact energy in relation to the specification and Sample W60 fell short of the strength requirement as well. All samples had acceptable percent elongation and similar reduction in area values.

## **B. MICROSTRUCTURAL CHARACTERIZATION**

### **1. Solidification Microstructure**

Figures 9-12 are montages constructed of optical micrographs taken using Oberhoffer's solution to show the dendritic solidification structure for each sample. The coarse beads of Samples W6 and W60 are indicative of the higher heat input associated with them as compared to the finer beads of Samples W2 and W58. Figures 9-12 all show dendritic growth from the fusion line toward the centerline essentially perpendicular to the maximum temperature gradient in the weld pool. The solidification structure appears fine and equiaxed in the papilla and in the corners near the fusion line where the cooling rate is expected to be the highest. Growth appears more cellular and primarily vertical at the centerline, especially visible in Figure 12. Some banding, probably banding of martensite [Ref. 12], parallel to the fusion line is also visible, particularly within the papilla.

A 2% Nital etchant was used in preparing Figures 13 and 14 which are optical micrograph montages showing the

grain solidification structure for samples W58 and W60, representative of each heat input. Large columnar grains growing perpendicular to the fusion line can be seen in both figures; the grains are finer in the papilla due to a higher cooling rate. These grains probably formed epitaxially from the austenite grains just outside the fusion line of the last weld pass. Some grain refinement in the HAZ (weld metal from previous passes) is visible, particularly near the papilla in Figure 13. Some smaller, equiaxed grains are visible right at the top of the weld pass in Figure 14, possibly due to the heterogeneous nucleation of new austenite grains on non-metallic inclusions near the surface of the weld [Ref. 12]. In contrast, the nearly vertical grains near the centerline are wide and very long in both grain structure montages.

## 2. Optical and Scanning Electron Microscopy

Optical microscopy showed very few differences between the microstructures of the four samples, hence only one representative optical micrograph taken near the center of the highest numbered weld pass for each sample is included in this report. On the other hand, some refinements in the microstructure can be seen by SEM so one micrograph at approximately 2000X for each sample at the low, average and high hardness is presented.

### a. Sample W2

Figure 15 is an optical micrograph of Sample W2 showing the primarily fine martensitic microstructure of the

weld. Some polygonal ferrite (the small white islands) can be seen and bainite may also be present, but it could not be readily distinguished by the etching treatment.

SEM analysis revealed the martensitic structure more clearly with some prior austenite grain boundaries visible along with a dispersion of carbides throughout the microstructure. Figures 16-18 were taken near the lowest, average and highest recorded Vickers microhardness indentations of Sample W2. The matrix in Figure 18 (highest hardness) appears significantly finer than the matrix in Figure 16 or 17, while the morphology in Figures 16 and 17 seems to be similar. The arrows and the "GB" in Figures 16 and 17 indicate visible prior austenite grain boundaries. The triangular shaped regions in Figure 16 are packets containing parallel laths of martensite. The dark polygonal regions visible could be polygonal ferrite.

#### b. Sample W6

The optical micrograph of Sample W6 presented as Figure 19 shows a coarser microstructure with more polygonal ferrite than in Figure 15 for Sample W2. The acicular morphology is not as pronounced as it is in Figure 15. Figures 20-22 are SEM micrographs similar to the SEM micrographs for Sample W2, but any microstructural refinement existing along the low to high hardness range is not as visible here. An inclusion (I) can be seen in Figure 21.

### c. Sample W58

Figure 23, an optical micrograph of Sample W58, is similar to Figure 19 for Sample W6. Again, a primarily martensitic microstructure with some polygonal ferrite was observed. SEM micrographs of Sample W58, Figures 23-26, show refinement of the microstructure corresponding to increases in microhardness; grain boundaries and inclusions are also visible in these micrographs. Figure 26 shows very well defined martensitic laths.

### d. Sample W60

No significant differences between Figure 27, an optical micrograph of Sample W60, and the optical micrographs for Samples W6 and W58 at 500X are visible. However, Sample W2 seems to have a finer microstructure and contained less polygonal ferrite than the other three. The finer morphology associated with higher microhardness is apparent again in Figures 28-30. More grain boundaries can be seen and the largest inclusion observed at 2000X is visible in Figure 29.

## 3. Transmission Electron Microscopy

TEM analysis was conducted to further understand and characterize the weld metal microstructures present in the four samples. The observation and quantification of microstructural differences relied heavily on TEM because optical and SEM analyses were inconclusive. The TEM micrographs at 15,000-54,000X presented here are representative of the microstructures observed.

a. Sample W2

Thin foil electron micrographs for weld pass #14 revealed a predominantly martensitic microstructure (dislocated lath and twinned martensite) with a high density of non-metallic inclusions and a large amount of retained austenite located preferentially between the lath boundaries. Small amounts of bainite, autotempered martensite and polygonal ferrite along with islands of tempered high carbon martensite and/or martensite-austenite particles were also present. An examination of weld pass #13 showed a similar microstructure, except no islands of tempered high carbon martensite were observed (this was the last weld pass so it received no thermal cycling from subsequent weld passes).

Figures 31 and 32 are micrographs from weld pass #13 of Sample W2. Figure 31 illustrates an island of polygonal ferrite between highly dislocated martensite/ferrite laths. The double arrows in Figure 32 point to second phase particles, probably martensite-austenite or high carbon martensite. These second phase particles seemed to exist predominantly along lath boundaries and at triple point junctions in the matrix.

Figures 33-40 are TEM micrographs of various microstructures observed in weld pass #14. Packets of parallel, highly dislocated laths of martensite separated by low angle grain boundaries can be seen in Figure 33. A second phase, probably retained austenite, was observed

between the laths. The ferrite laths perpendicular to the martensite packet in the center of Figure 33 appear to have nucleated on the two inclusions near the right. The second phase between the laths is better resolved in Figure 34 due to the higher magnification. A cluster of inclusions can be seen in Figure 35; they are most likely primarily manganese and silicon oxides formed during the welding process [Ref. 12]. Figure 36 clearly shows lower bainite with the intragranular cementite (C) particles exhibiting a preferred crystallographic orientation. The double arrows in the upper left point to a dark colored second phase region, probably high carbon tempered martensite (tempered by the thermal cycling experienced in this weld pass).

Figure 37 illustrates some twinned martensite (T), more common within the microstructure of Sample W2 than any other sample. These twins appear to be located on or near a prior austenite grain boundary. Figure 38 shows a high magnification view of the carbon rich second phase, probably tempered martensite, identified previously in Figure 36. Figures 39 and 40 are bright and dark field TEM micrographs included to confirm the presence of retained austenite between the ferrite laths.

#### **b. Sample W6**

Sample W6 exhibited a predominantly bainitic microstructure with some large autotempered martensite laths containing fine cementite particles within the laths and a

high density of inclusions. Smaller amounts of martensite-austenite particles, dislocated lath martensite, retained austenite and lath ferrite were also observed. Figure 41 shows single ferrite laths essentially perpendicular to adjacent packets of lath ferrite. Figure 42 illustrates autotempered martensite with some twinned martensite. The double arrows in Figure 43 denote the location of a second phase, probably martensite-austenite. Figure 44 shows twinned martensite and a large spherical inclusion.

#### c. Sample W58

The primarily bainitic microstructure observed for Sample W58 contained a large number of second phase particles, significant amounts of retained austenite between the ferrite laths and some lath martensite. The ferrite laths were decorated with the second phase particles, assumed to be martensite-austenite or high carbon martensite. Sample W58 also had a significantly lower inclusion density than either Sample W2 or W6 and it contained very little autotempered martensite. Figure 45 depicts a lath ferrite structure with a high dislocation density and several second phase particles as marked by the double arrows. Figure 46 shows a stringer of various sized inclusions along with a rare completely twinned martensite lath. Figures 47 and 48 are bright and dark field micrographs of one location included to show the presence of retained austenite between the martensite/ferrite laths.

**d. Sample W60**

Sample W60 had a bainitic microstructure with a large amount of lath ferrite, coarser than observed for any other sample. The inclusion density was similar to Sample W58, but much lower than seen in Samples W2 and W6. Sample W60 also had more autotempered martensite than Sample W2 or W58. Parallel ferrite laths separated by small regions of retained austenite are visible in Figure 49. Some of the ferrite laths in Figure 50 may have nucleated on the spherical inclusions shown. Figure 51 clearly illustrates autotempered martensite, most frequently observed in the higher heat input weldments (W6 and W58), along with some twins. Figure 52 illustrates a lower bainite structure on the right side of the micrograph with cementite precipitated within the lath. However, the lower bainite observed here is not as clearly defined as in Figure 36 for Sample W2.

**e. TEM Microstructure Summary**

A relative order of microconstituents observed in the four samples was determined based on a qualitative TEM analysis. The results of this analysis are presented as Table 7. The quantities associated with each sample are based on a comparison of relative amounts between the samples using at least five foils for each, not on quantitative measurements of the fractions of the microconstituents present. This summary does not provide conclusive evidence of the microstructure present for the entire weld of each

TABLE 7  
SUMMARY OF TEM MICROSTRUCTURAL ANALYSIS

Microconstituent	Sample W2	Sample W6	Sample W58	Sample W60
<b>Lath Martensite</b>	<b>High</b>	<b>Low</b>	<b>Medium</b>	<b>Very Low</b>
<b>Retained Austenite</b>	<b>High</b>	<b>Medium</b>	<b>High</b>	<b>Medium</b>
<b>Twinned Martensite</b>	<b>High</b>	<b>Low</b>	<b>Medium</b>	<b>Very Low</b>
<b>Islands of High Carbon Martensite and/or Martensite-Austenite</b>	<b>High</b>	<b>Very Low</b>	<b>High</b>	<b>Very Low</b>
<b>Autotempered Martensite</b>	<b>Very Low</b>	<b>High</b>	<b>Very Low</b>	<b>Low</b>
<b>Bainite/Lath Ferrite</b>	<b>Medium</b>	<b>Medium</b>	<b>Medium</b>	<b>High</b>
<b>Polygonal Ferrite</b>	<b>Very Low</b>	<b>Low</b>	<b>Very Low</b>	<b>Low</b>
<b>Non-Metallic Inclusions</b>	<b>High</b>	<b>High</b>	<b>Low</b>	<b>Low</b>

sample, but it does represent an accurate analysis for the last weld pass of each sample.

#### 4. Inclusion Size

Approximately 100 inclusions, ranging in size from 0.16 - 1.26  $\mu$ s, were measured for each sample from TEM micrographs. The values measured were grouped into blocks 0.1  $\mu$  wide for the histograms presented as Figures 51-54. The histograms show Sample W2 had the smallest average size and the smallest size range. Sample W6 exhibited the largest average sized inclusions, while Sample W58 had the largest size range.

## V. DISCUSSION

The primary emphasis of this study was to identify microstructural differences between the four weldments examined. Optical microscopy and SEM did not prove particularly revealing in characterizing the fine microstructures present in the weld metal. Microstructures appearing very similar by optical and SEM metallography were often quite different when observed by TEM. Hence, TEM observations are heavily relied upon in this analysis of the results.

### A. MICROSTRUCTURE

The microstructure observations for all four samples are in general agreement with observations of other HY-130 researchers. A lath martensite/ferrite structure with thin film interlath retained austenite and some twinned martensite with no carbides between the laths was observed in various volume fractions in all four weldments (Table 7). This structure is similar to the HY-130 weld metal microstructures observed by Challenger et al. [Ref. 2]. Although twinned martensite is generally seen only when the carbon content is greater than 0.15 wt%, its presence in these HY-130 weldments (carbon content <0.10 wt%) can be explained. Challenger et al. [Ref. 2] attributed twinned martensite observed in HY-130 weld metal to carbon segregation during transformation.

Islands of high carbon tempered martensite were observed only in weld pass #14 (the next to the last pass) of Sample W2 due to thermal cycling from pass #13. This tempering should improve ductility and increase toughness as compared to weld pass #13 (the last pass). Only the final weld pass of each of the other samples was observed using TEM, so tempered martensite was not searched for in other samples.

Thin films of interlath retained austenite were detected in TEM micrographs of all four samples. Thomas [Ref. 8] also reports observations of retained austenite existing as very thin films between the martensite laths only by TEM. A microduplex structure of lath martensite and thin film interlath retained austenite was reported to produce a good combination of strength and toughness in Fe/Cr/C base steels [Ref. 18]. This structure, observed most significantly in Sample W2 (Table 7), appears to be responsible for the high strength and toughness recorded for Sample W2 (Table 6). Analysis of weld pass #14 of Sample W2 showed relatively high amounts of interlath retained austenite (similar to pass #13) suggesting that the retained austenite present is essentially stable under significant thermal cycling conditions.

The effect of retained austenite on hydrogen assisted cracking in martensitic steels is still controversial. Kim et al. [Ref. 21] associated increased susceptibility to hydrogen embrittlement with the presence of unstable interlath retained austenite. Ritchie et al. [Ref. 20]

report that retained austenite reduces SCC crack velocity by lowering susceptibility to hydrogen embrittlement. Based on the higher amounts of retained austenite observed in Samples W2 and W58 (Table 7), the lower heat input may produce a lower susceptibility to hydrogen embrittlement, assuming the retained austenite is stable as indicated above.

Palko et al. [Ref. 15] suggested a tempered microstructure containing a minimum of 60-75% martensite to achieve the specified properties for HY-130 steel. Sample W2 contained the highest percentage of martensitic structures which appears to correlate well with the attainment of the specified strength and toughness.

Glover et al. [Ref. 6] report that poor impact toughness in welds may be compounded by the formation of high carbon martensite-austenite particles on ferrite boundaries where they can act as efficient crack nucleation sites. Sample W2 exhibited good toughness in spite of the observation of significant amounts of martensite-austenite particles and islands of high carbon tempered martensite along lath boundaries. However, the toughness of Sample W2 might have been higher if the martensite-austenite particles had comprised a lower volume fraction.

The observation of higher amounts of twinned martensite in Sample W2 may be the main area of concern in choosing Sample W2 as the best weldment of the four studied. Chen et al. [Ref. 16] have identified twinned martensite as one of

the microstructures most susceptible to hydrogen induced cracking and SCC. Although the strength and impact toughness of Sample W2 are far superior to the other three samples, the desirability of this weld in service may be reduced by possible hydrogen related and SCC problems.

#### **B. EFFECT OF HEAT INPUT**

The lower heat input (higher cooling rate) produced finer microstructures, more low temperature transformation products, less ferrite and less autotempered martensite (Table 7). The welds with higher cooling rates (Samples W2 and W58) had significantly more lath martensite and retained austenite than the other two. This observation is in agreement with several previous reports [Refs. 6, 10 and 22]. ASTM Publication 494 [Ref. 24] specifies a minimum cooling rate of  $16.7^{\circ}\text{C/sec}$  for HY-130 to provide acceptable yield strength in the weld metal. Samples W6 and W60 (cooling rate of  $13.0^{\circ}\text{C/sec}$ ) were slightly below the minimum specified cooling rate which provides one reason for the lower yield strengths measured for these weldments.

From Table 6, the lower heat input can be associated directly with higher yield strength. Relatively high amounts of very hard high carbon martensite and/or martensite-austenite were observed in the low heat input samples. Biss and Cryderman [Ref. 9] report that martensite-austenite can cause poor impact properties and lower yield strength in low carbon steels. It is not possible to draw a similar

conclusion from the results of this analysis since no obvious trend in toughness was observed and the higher martensite-austenite volume fractions were associated with higher yield strengths. However, the presence of higher amounts of martensite-austenite may explain the relatively high microhardness values measured for Sample W58.

The larger number of weld beads in a similar cross-sectional area resulting in additional thermal cycling at the higher cooling rate contributed to microstructural refinement and a more uniform hardness in the weld metal for Samples W2 and W58. The refinement and homogenization provided by thermal cycling should improve mechanical properties and promote ductile fracture [Ref. 16]. Tempering treatment provided by multipass welding (most significant at lower heat inputs) may increase impact energy and yield strength associated with the precipitation of fine, intralath carbides from the martensite [Ref. 18]. If any carbides existed in the tempered martensite observed in weld pass  $\pm 4$  of Sample W2, they were not resolved by TEM. However, fine intralath carbides were observed in the autotempered martensite microstructure most prevalent in Sample W6. Temper embrittlement often observed near 260°C is due to the precipitation of film-like carbides on prior austenite grain boundaries and sub-boundaries [Ref. 19]. Although no tests were conducted to determine temper embrittlement, this may

not be a problem in any of the samples because no carbides were observed between the laths.

The higher cooling rate may be responsible for the higher amounts of retained austenite observed in Samples W2 and W58. This observation is based on the findings of Sarikaya et al. [Ref. 18] who report that multiple heat treatments provided by thermal cycling from subsequent weld passes can produce a compositionally homogeneous structure, grain refinement and increased amounts of retained austenite.

Connor et al. [Ref. 17] report lower porosity and lower hydrogen entrapment as additional benefits of a lower heat input based on a shallower weld pool and shorter diffusion distances. Porosity and hydrogen content were not measured in this study, but they are assumed lower in Samples W2 and W58 based on the observations of Connor et al.

### C. EFFECT OF COMPOSITION

The carbon and oxygen contents seem to be the most significant differences between the two electrodes used in this analysis (Table 2). The higher carbon content of electrode Linde 151140 is expected to lower the  $M_a$  temperature and push the austenite transformation to longer times. According to Easterling [Ref. 5], austenite stabilizers (C, N, Mn, Ni, Cu) push transformation to longer times and enhance the formation of low temperature products such as bainite and martensite. The  $M_a$  temperatures, based

on the electrode compositions using Andrews' empirically determined formula [Ref. 26], are as follows:

- \* Electrode Linde 151140  $M_s = 403.5^{\circ}\text{C}$
- \* Electrode LTEC 140005  $M_s = 421.1^{\circ}\text{C}$

A lower  $M_s$  temperature enhanced the formation of martensite and helped stabilize the austenite so more retained austenite was observed in Samples W2 and W6. The lower  $M_s$  temperatures obtained using electrode Linde 151140 should also produce a finer microstructure.

The higher oxygen content of electrode Linde 151140 is assumed responsible for the significantly higher density of non-metallic inclusions observed in Samples W2 and W6 as compared to Samples W58 and W60. Grong and Matlock [Ref. 12] report that nucleation of acicular ferrite on inclusions is always more favorable than homogeneous nucleation, regardless of the inclusion size. The exact effect of this higher inclusion density is uncertain, but it appears that the inclusions may have acted as lath nucleation sites. Hence, microstructural refinement for Sample W2 as compared to Sample W58 and for Sample W6 as compared to Sample W60 may be explained.

The weld metal inclusions measured had average diameters less than 1 micron for all samples. This is similar to an observation previously reported by Grong and Matlock [Ref. 12]. They also report an increase in inclusion diameter with increasing heat input. Samples W6 and W60 (higher heat

input) had larger inclusions than Samples W2 and W58. Farrar and Harrison [Ref. 10] observed that smaller inclusions may pin austenite grain boundaries, thus restricting grain size and providing good nucleation sites for polygonal ferrite. Grong and Matlock [Ref. 12] report that inclusions with diameters from 0.4-1.0 micron are the most potent nucleation sites for acicular ferrite. No direct correlation of inclusion diameter with the amounts of acicular ferrite and/or polygonal ferrite formed were made in this study. Sarikaya et al. [Ref. 18] associated inferior toughness properties with a high density of large oxide particles in an air melted 2 wt% nickel alloy steel. The higher density of relatively large inclusions observed in Sample W6 acting as crack nucleation sites may be responsible for the lower impact toughness in this sample (Table 6).

## VI. CONCLUSIONS

- \* A microduplex structure of lath martensite and thin film interlath retained austenite is associated with higher strength and toughness in the thin section HY-130 weldments examined.
- \* The lower heat input (0.79 kJ/mm as compared to 1.61 kJ/mm) produced finer weld beads, microstructural refinement and a more uniform hardness.
- \* The electrode with a higher carbon content lowered the  $M_s$  temperature, assisted in the formation of more lath martensite and stabilized the austenite.
- \* Sample W2, exhibiting the highest strength and impact toughness of the four weldments examined, contained larger amounts of low temperature transformation products than the other samples. The lower heat input in combination with the higher carbon content electrode produced more of the microduplex structure than observed in any other sample.

## VII. RECOMMENDATIONS

This study concentrated on the effects of two welding variables. In order to develop a complete set of welding procedures for thin section HY-130 GMAW weldments, additional studies are needed. A detailed microstructural characterization of additional thin section HY-130 GMAW weldments fabricated with electrode Linde 151140 using at least three different heat inputs between 0.79 and 1.61 kJ/mm is required. This is particularly important in minimizing costs since larger weld beads mean fewer weld passes and less time spent in the welding process. The work performed by Connor et al. [Ref. 17] would provide significant assistance in designing additional studies based on the mechanical property results they have reported for a wide variety of thin section HY-130 weldments.

Based on the discussion concerning twinned martensite and retained austenite, several unanswered questions remain about the susceptibility of Sample W2 to SCC and hydrogen related problems. Therefore, a further study of the susceptibility of Sample W2 to hydrogen assisted cracking and SCC as compared to HY-130 base plate is also recommended. The work reported by Chen et al. [Ref. 16] would serve as a guide in planning this study.

## **APPENDIX**

### **FIGURES**

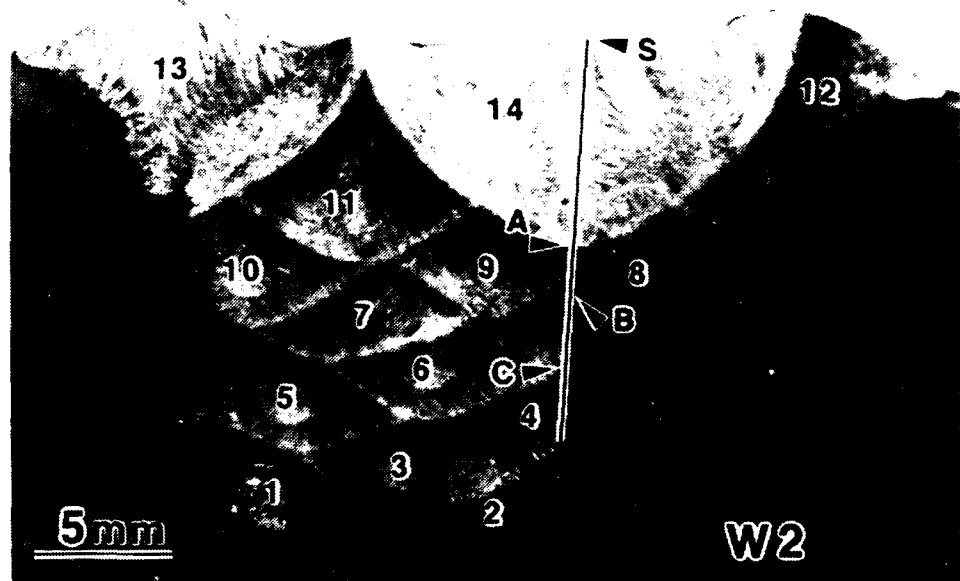


Figure 1. Macrosample of Weldment W2

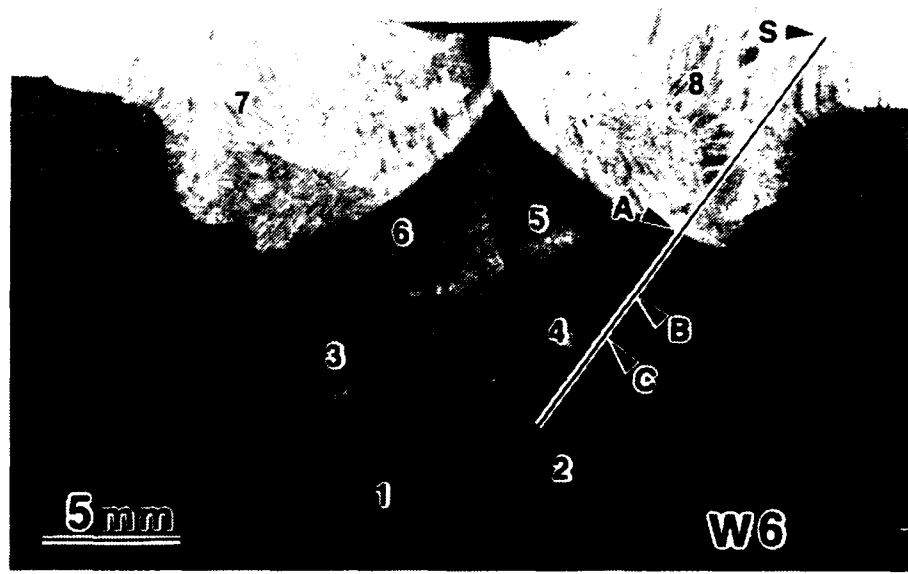
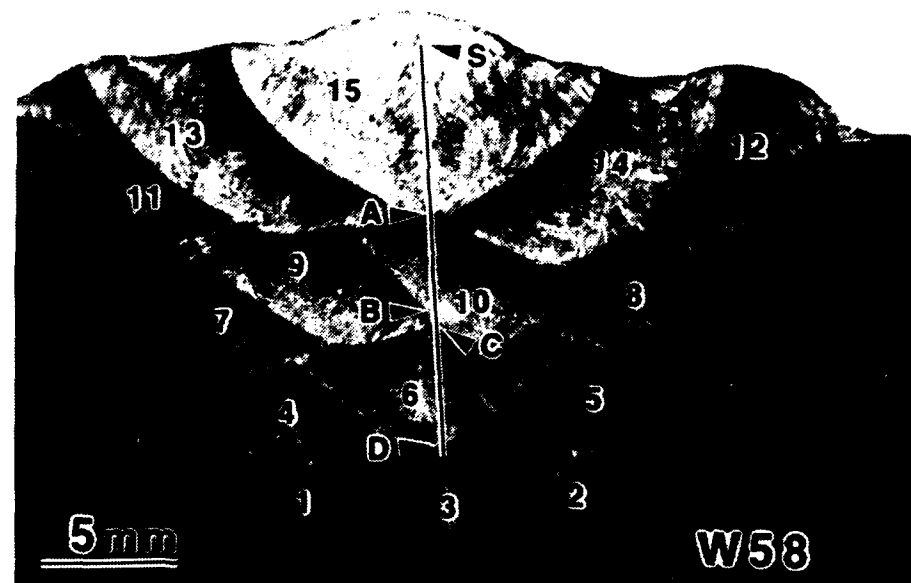


Figure 2. Macrosample of Weldment W6



**Figure 3. Macrosample of Weldment W58**



**Figure 4. Macrosample of Weldment W60**

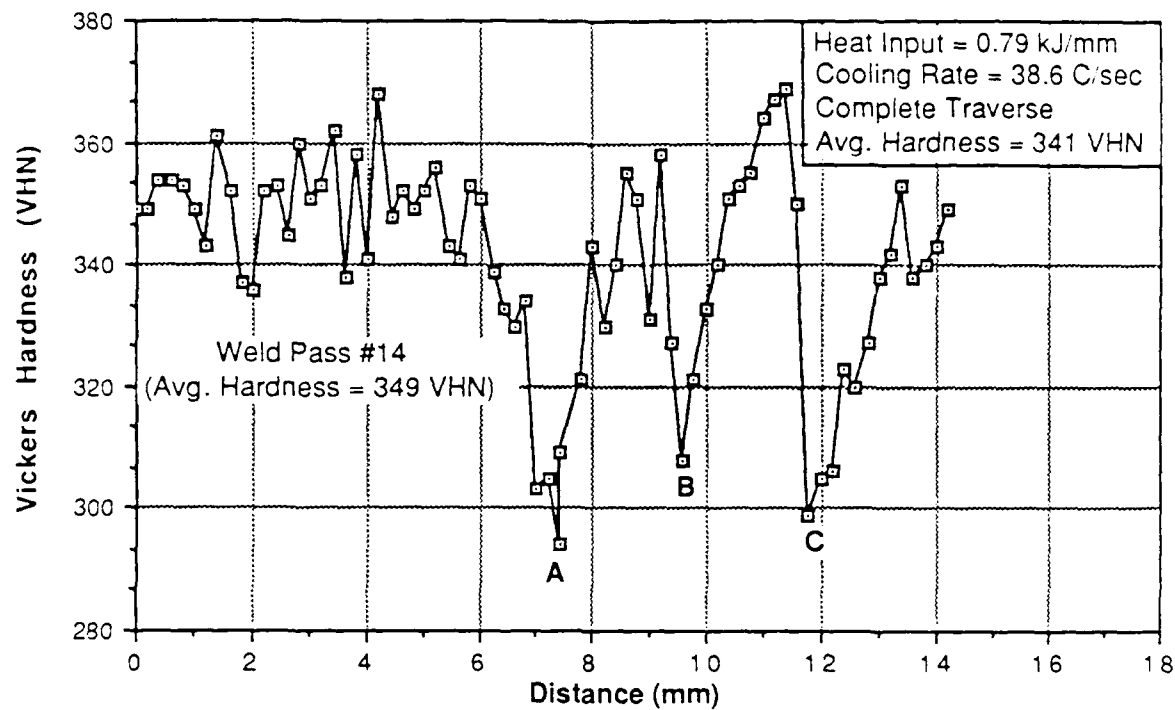


Figure 5. Microhardness Profile for W2

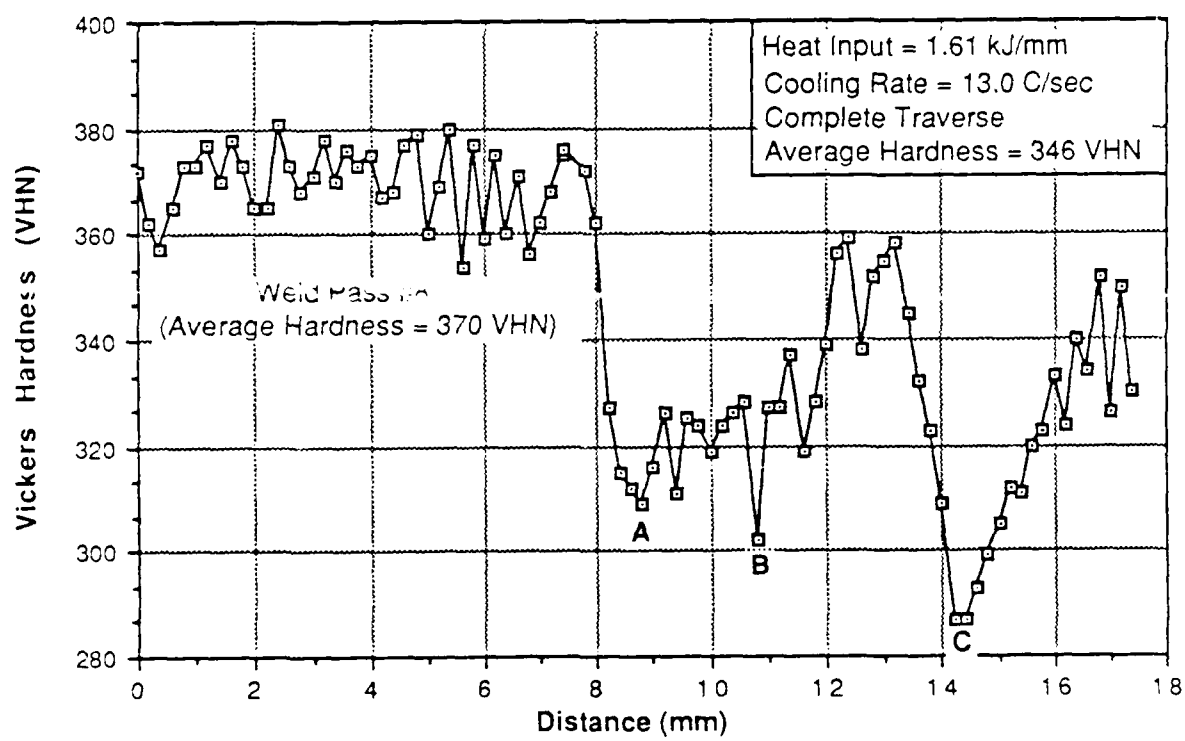


Figure 6. Microhardness Profile for W6

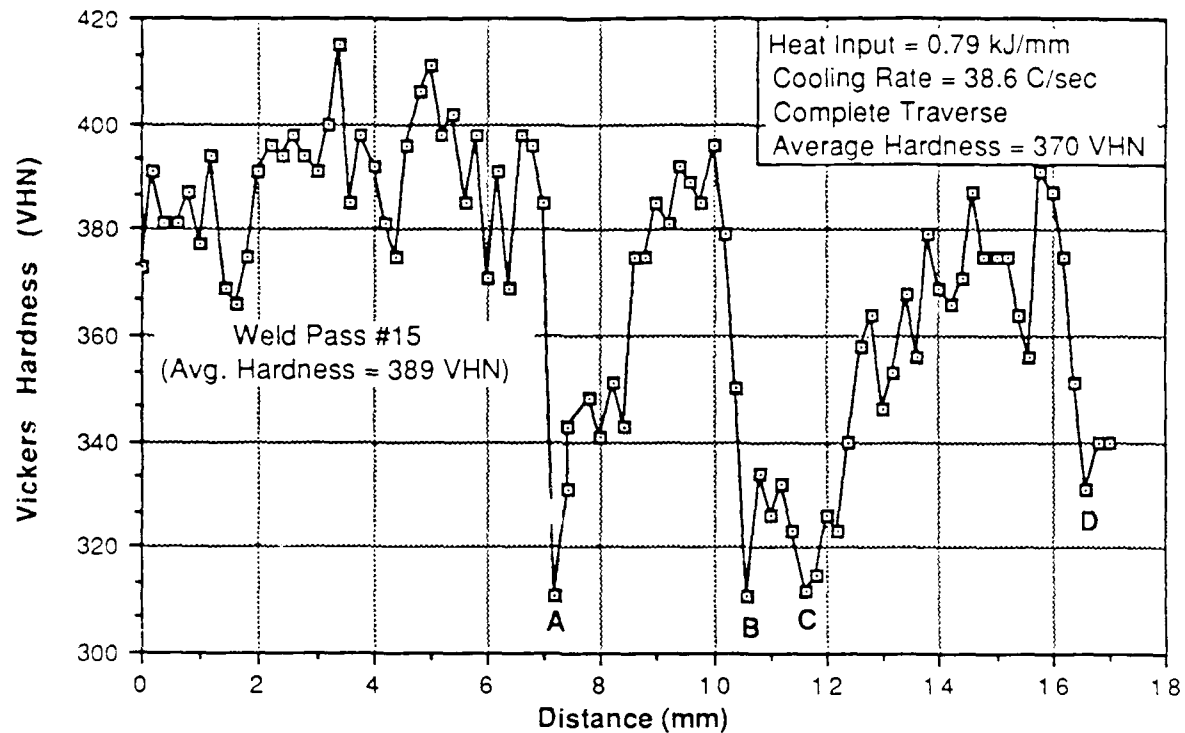


Figure 7. Microhardness Profile for W58

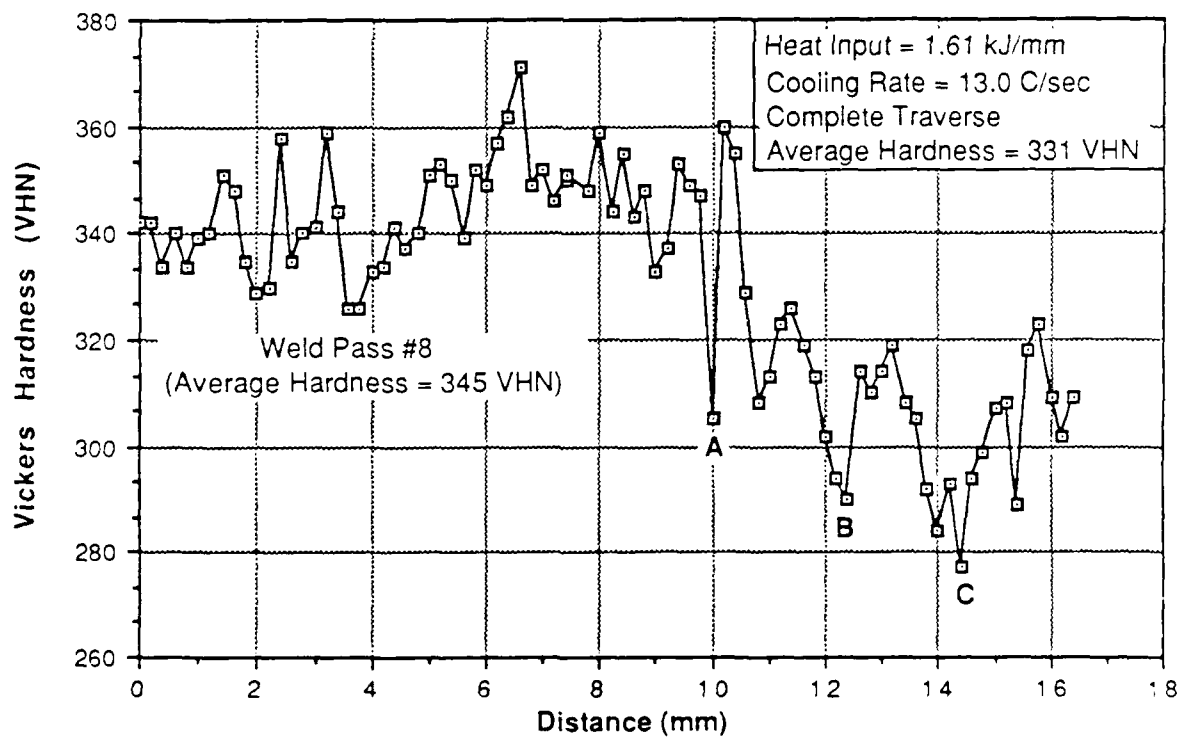


Figure 8. Microhardness Profile for W60



Figure 9. Dendritic Solidification Structure of Sample W2

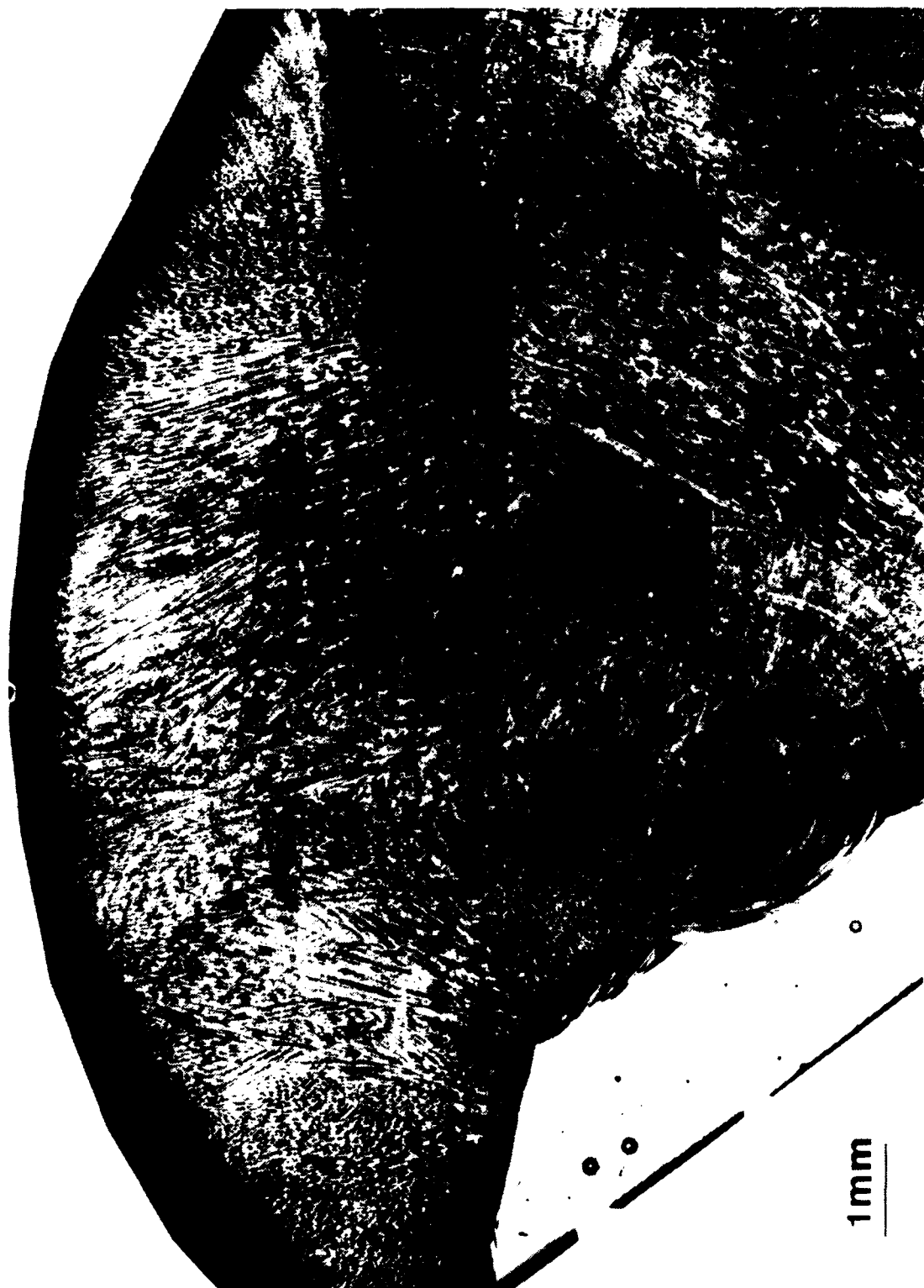


Figure 10. Dendritic Solidification Structure of Sample W6



Figure 11. Dendritic Solidification Structure of Sample W58

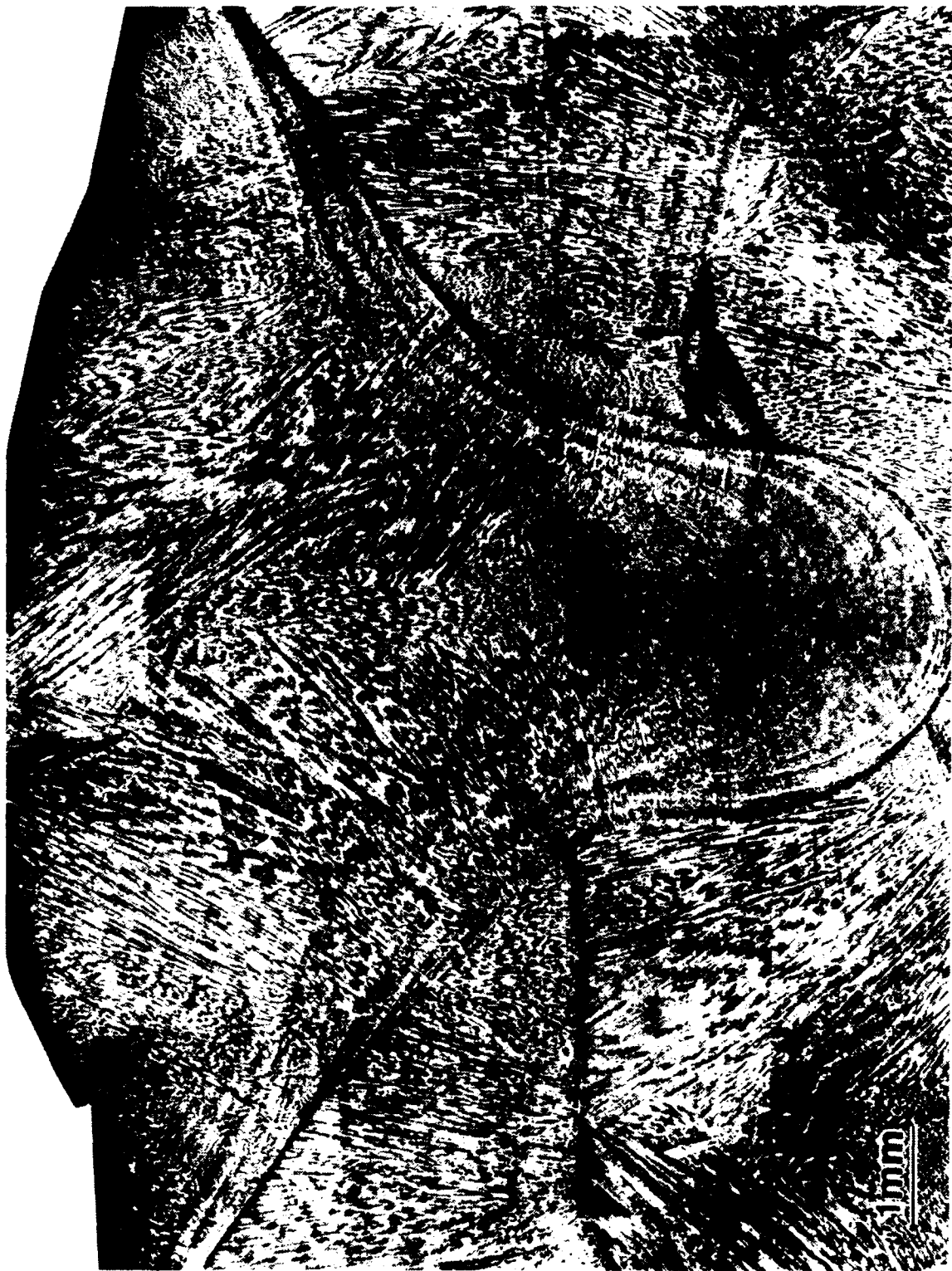


Figure 12. Dendritic Solidification Structure of Sample W60

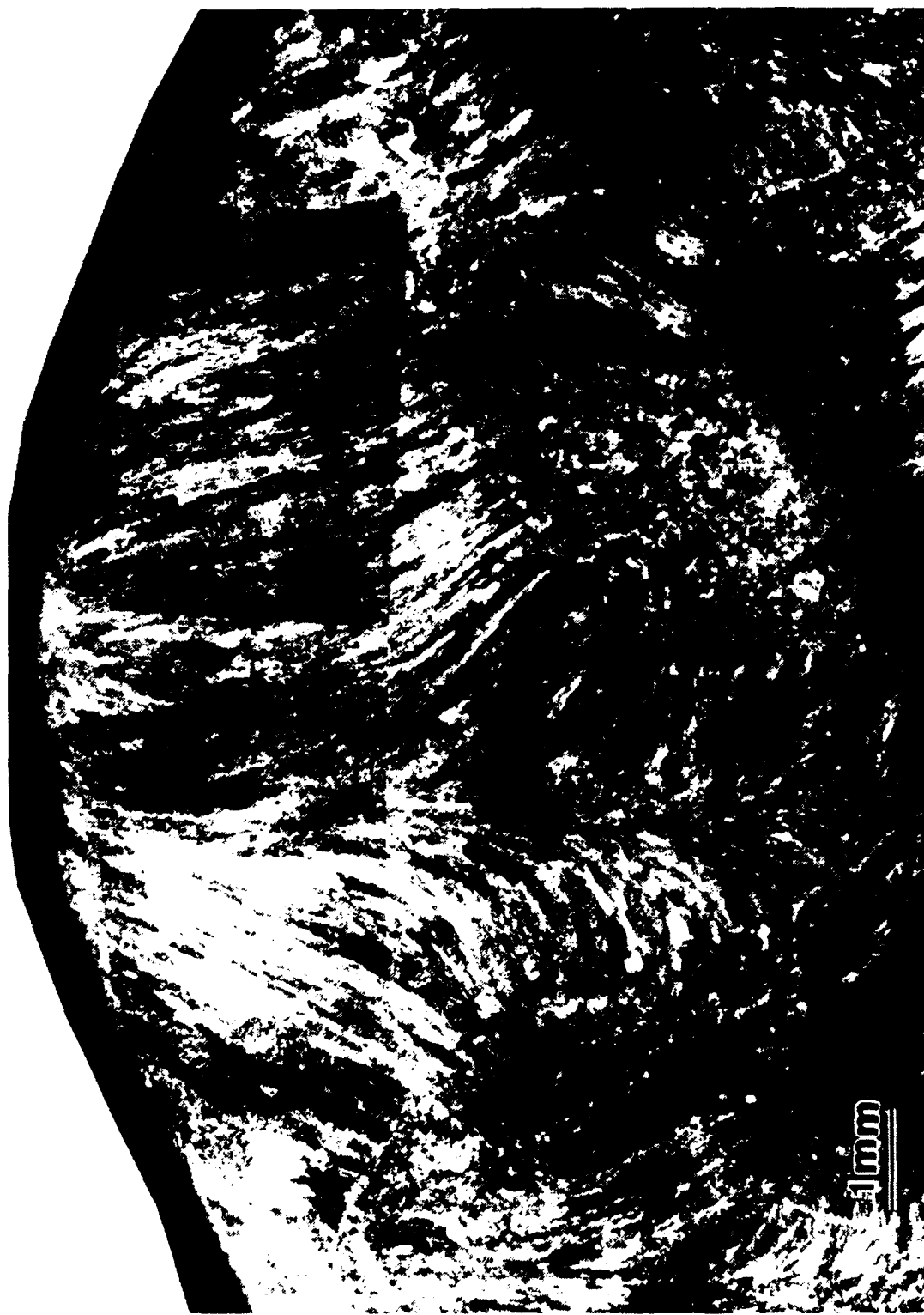


Figure 13. Grain Solidification Structure of Sample W58

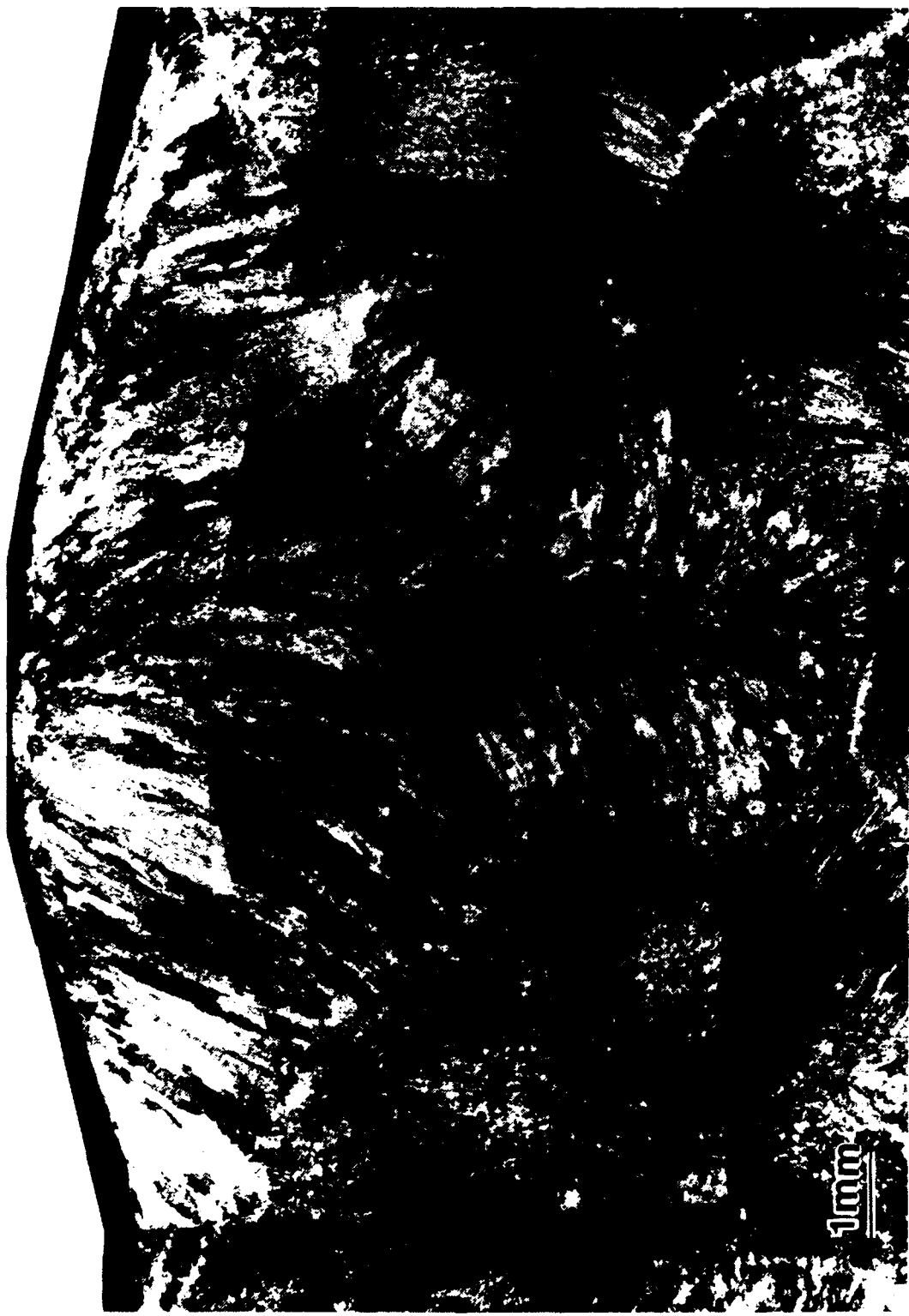


Figure 14. Grain Solidification Structure of Sample W60

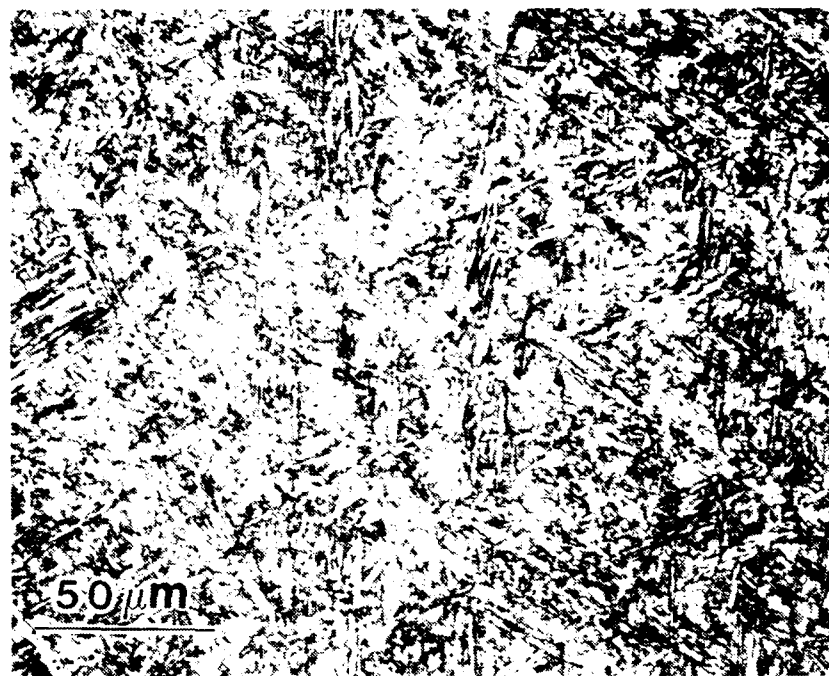


Figure 15. Optical Micrograph of Sample W2

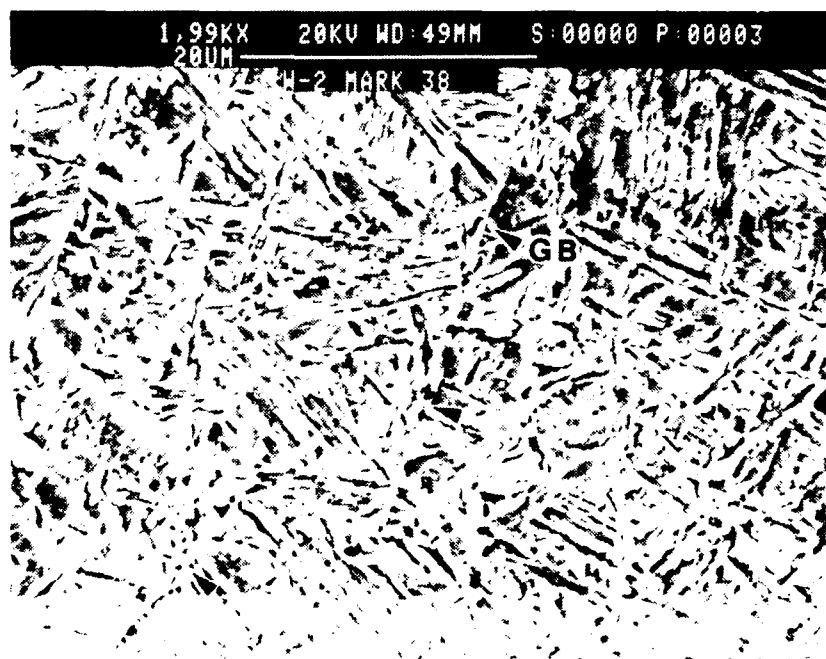


Figure 16. SEM Micrograph of Sample W2 (Low Hardness)

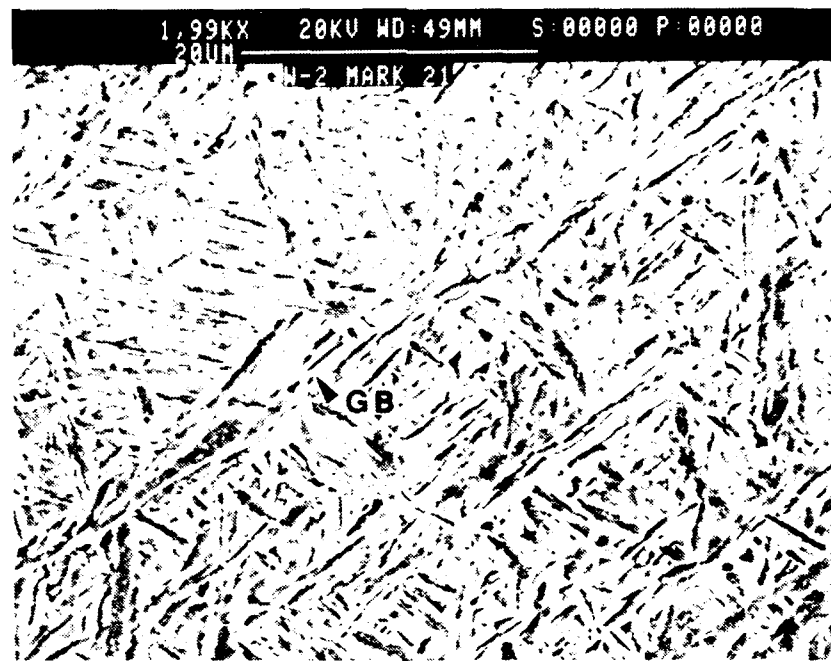


Figure 17. SEM Micrograph of Sample W2 (Average Hardness)

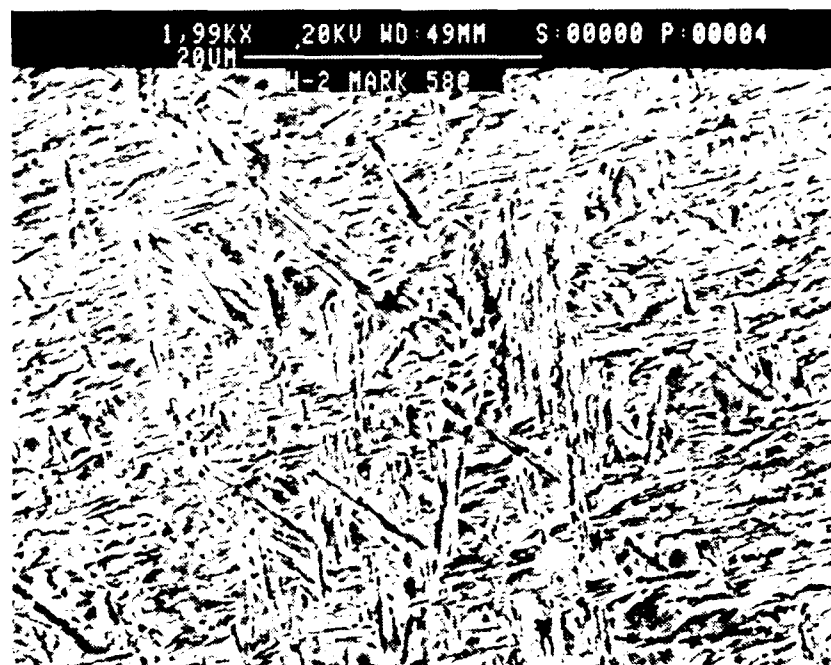


Figure 18. SEM Micrograph of Sample W2 (High Hardness)

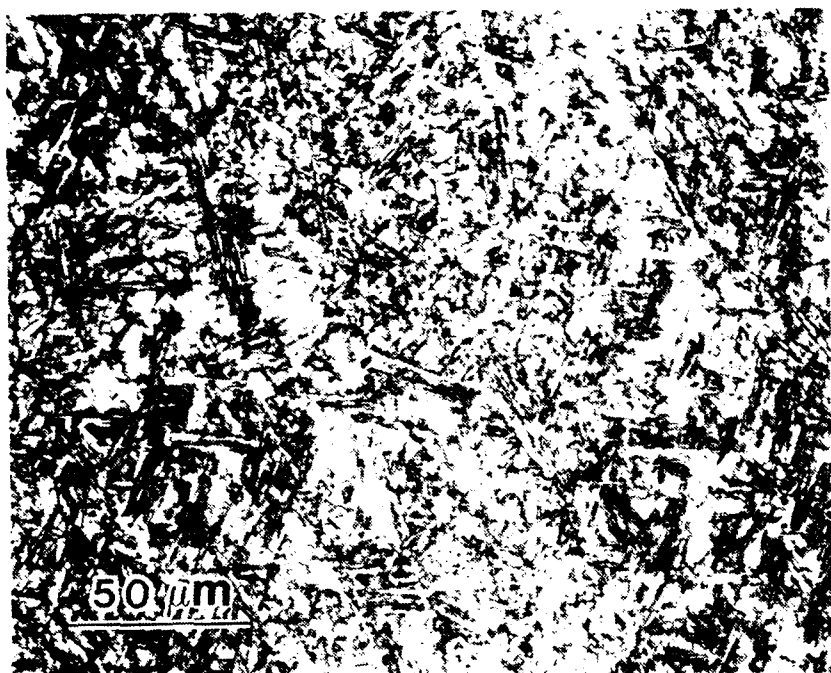


Figure 19. Optical Micrograph of Sample W6

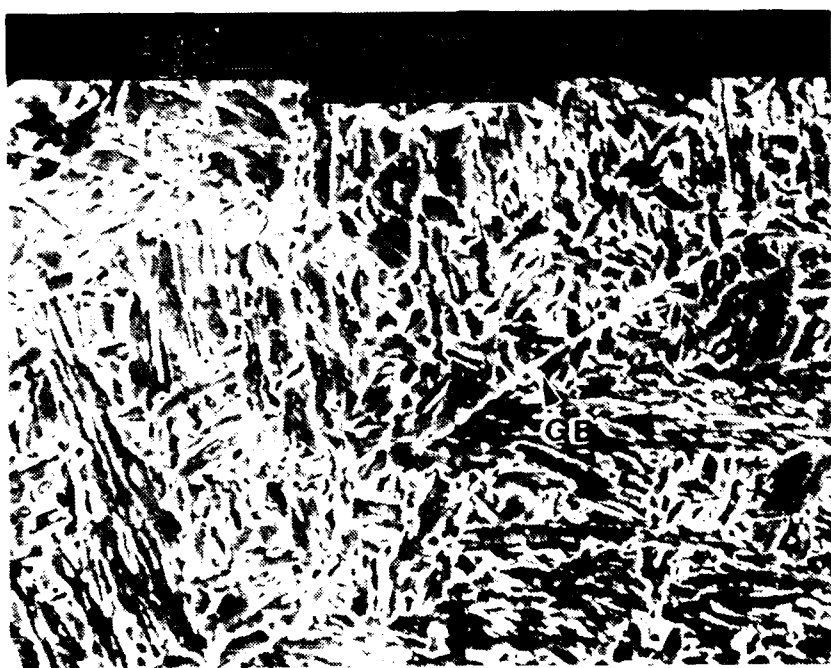


Figure 20. SEM Micrograph of Sample W6 (Low Hardness)



Figure 21. SEM Micrograph of Sample W6 (Average Hardness)

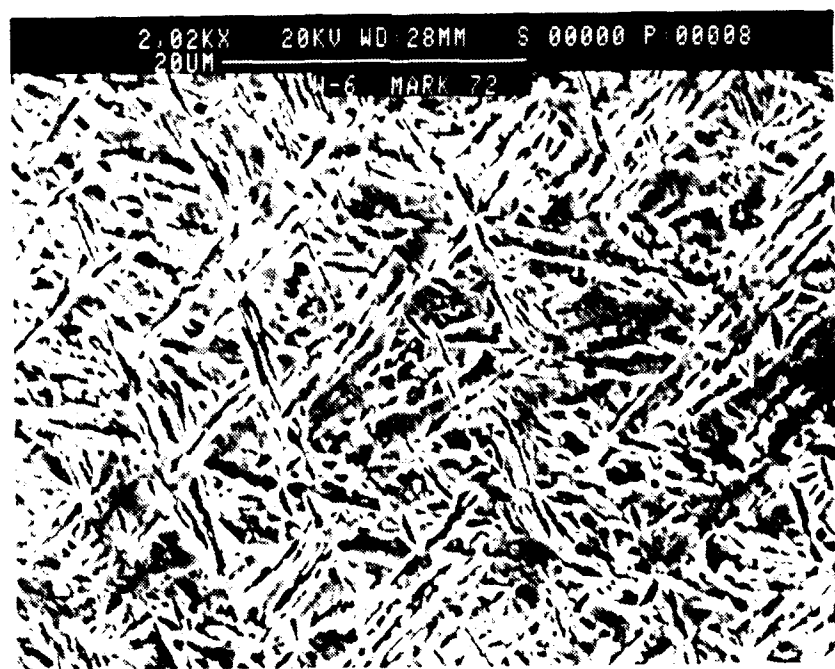


Figure 22. SEM Micrograph of Sample W6 (High Hardness)



Figure 23. Optical Micrograph of Sample W58

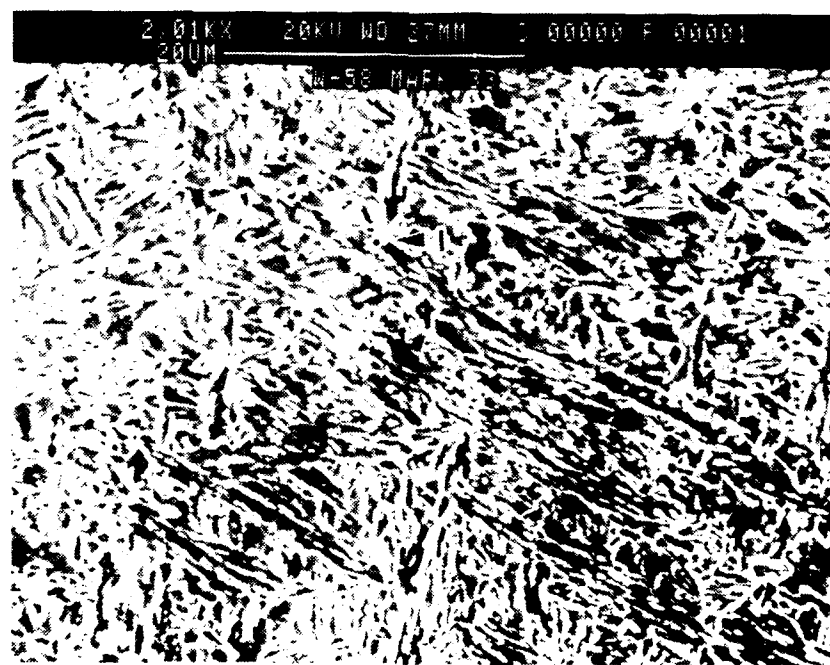
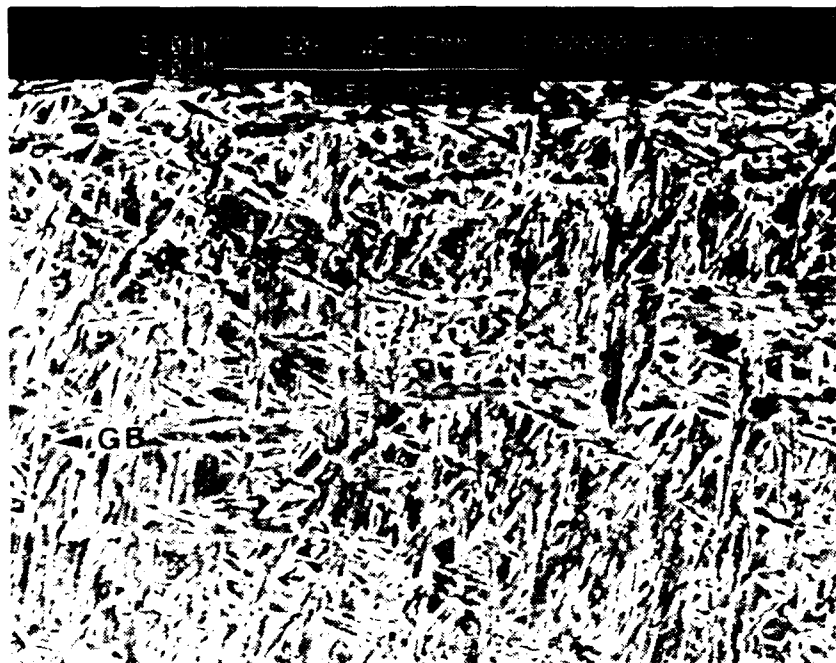
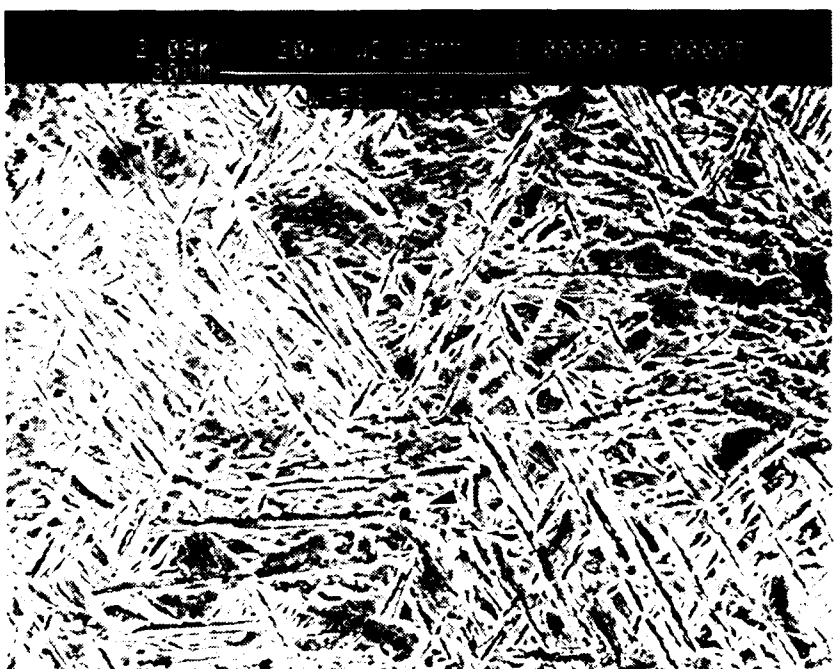


Figure 24. SEM Micrograph of Sample W58 (Low Hardness)



**Figure 25. SEM Micrograph of Sample W58 (Average Hardness)**



**Figure 26. SEM Micrograph of Sample W58 (High Hardness)**

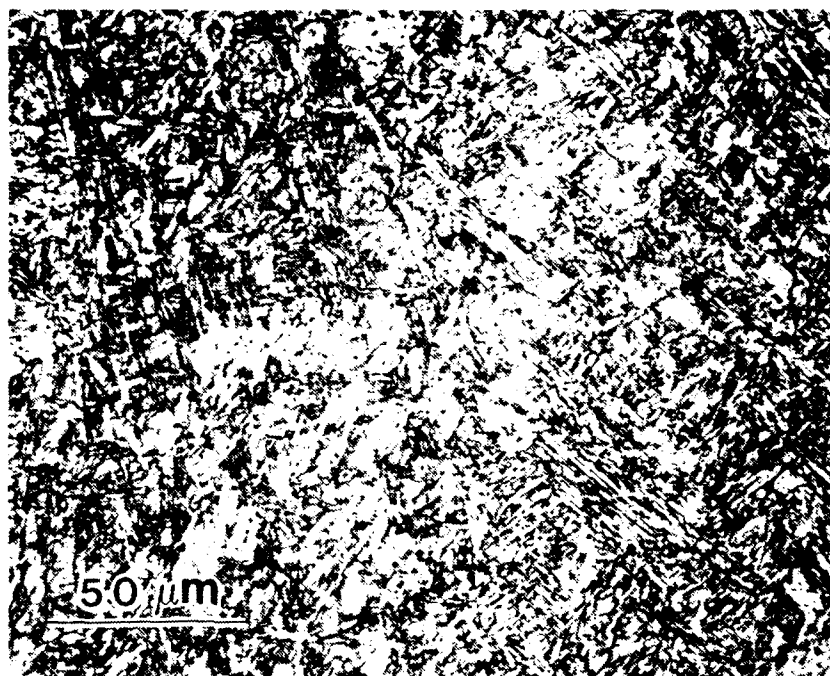


Figure 27. Optical Micrograph of Sample W60

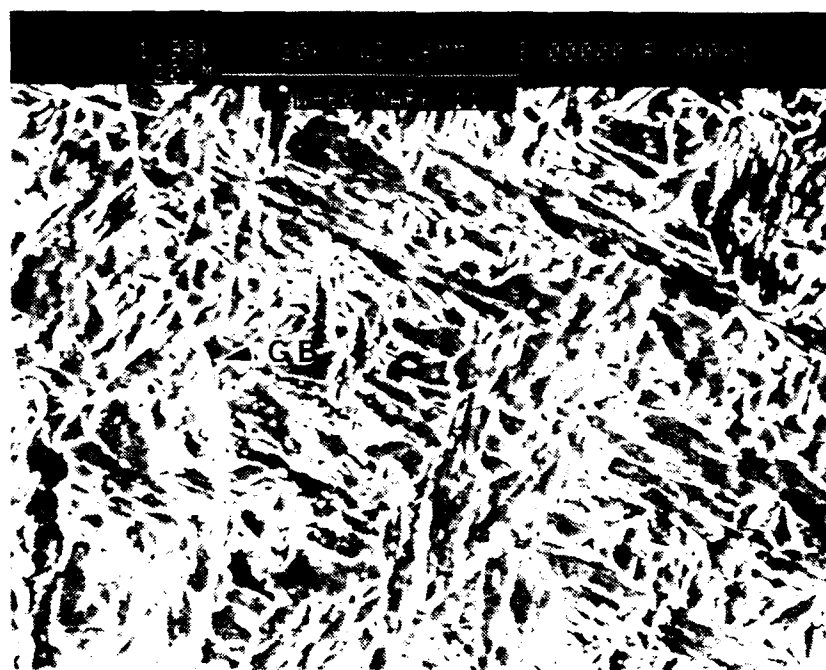


Figure 28. SEM Micrograph of Sample W60 (Low Hardness)

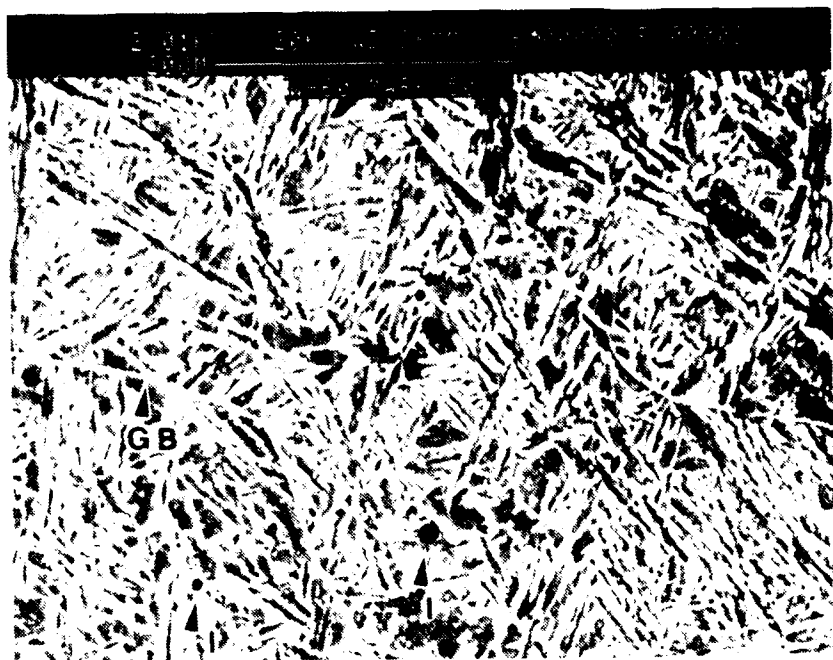


Figure 29. SEM Micrograph of Sample W60 (Average Hardness)

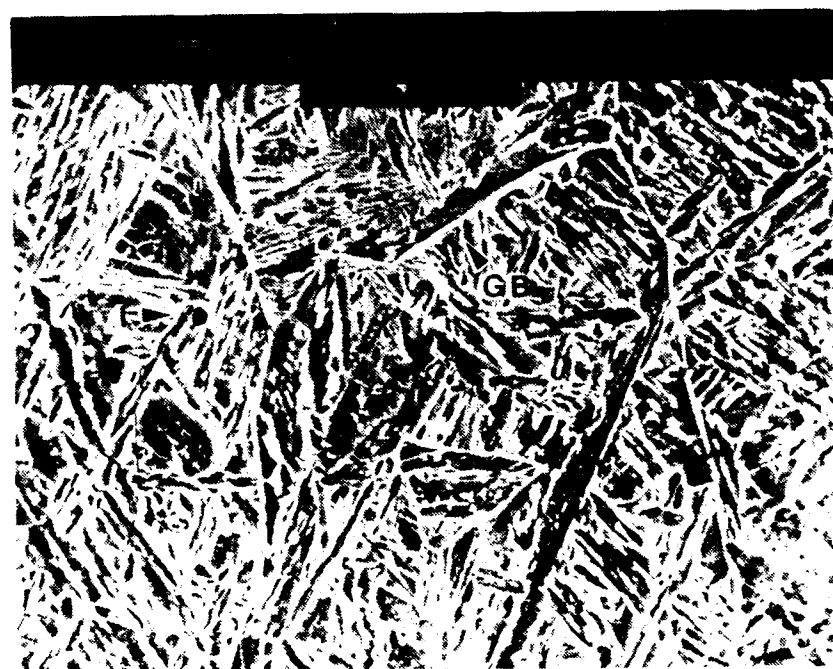


Figure 30. SEM Micrograph of Sample W60 (High Hardness)

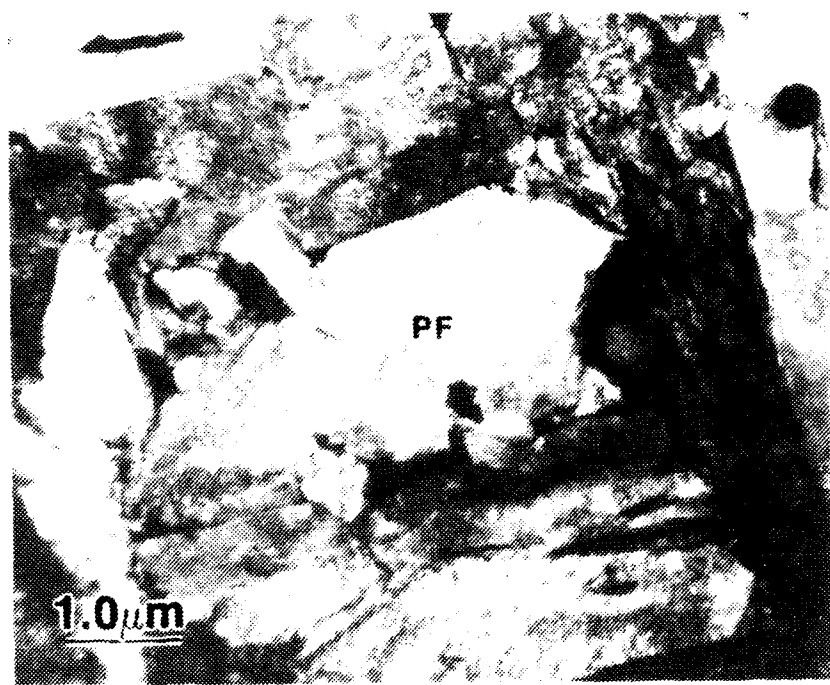


Figure 31. TEM Micrograph of Sample W2 (Pass #13)

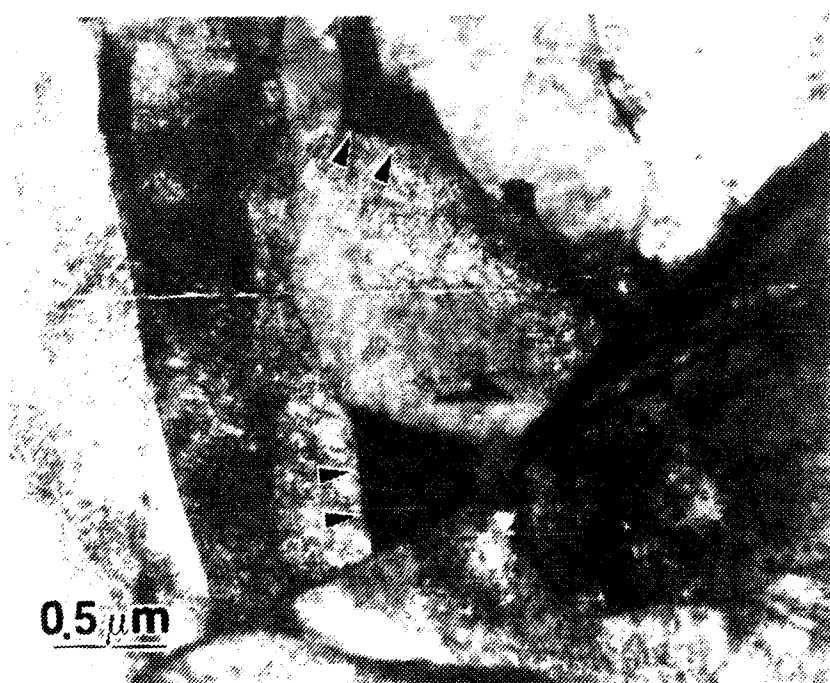


Figure 32. TEM Micrograph of Sample W2 (Pass #13)



Figure 33. TEM Micrograph of Sample W2 (Pass #14)

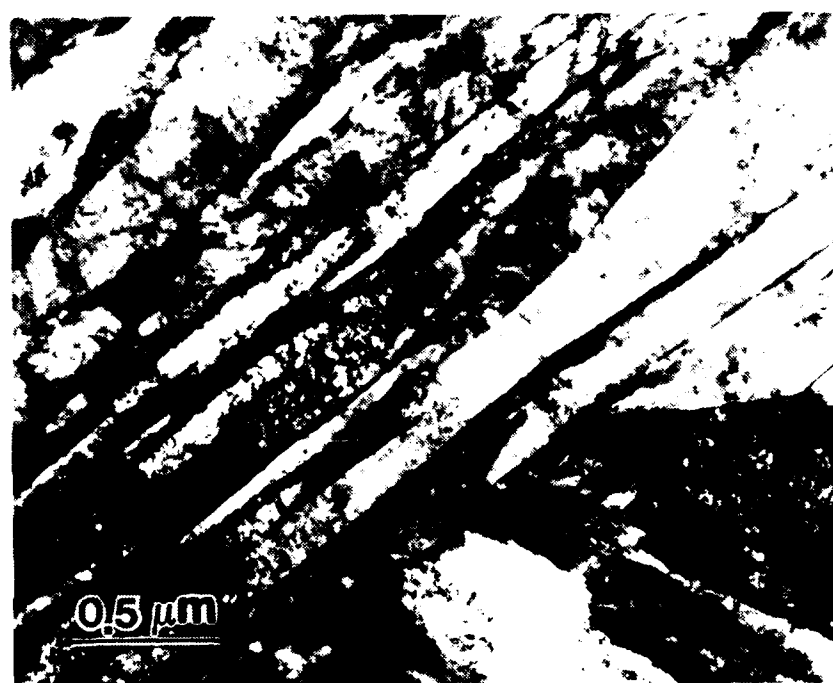


Figure 34. TEM Micrograph of Sample W2 (Pass #14)

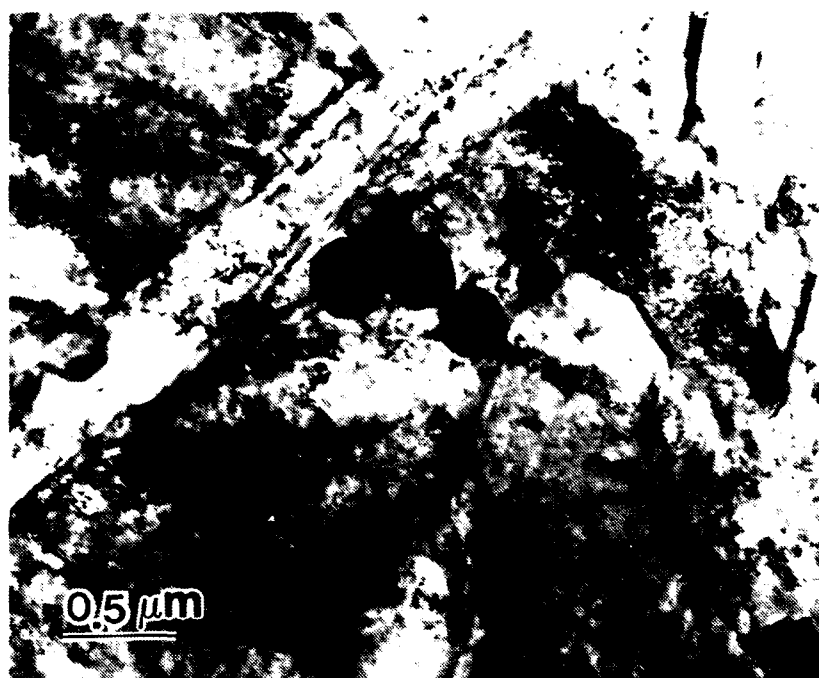


Figure 35. TEM Micrograph of Sample W2 (Pass #14)

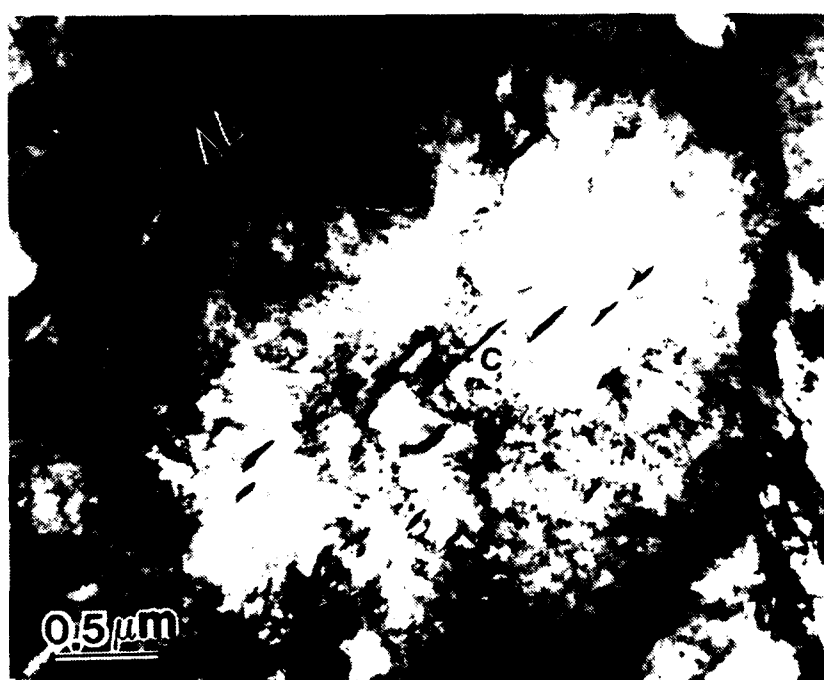


Figure 36. TEM Micrograph of Sample W2 (Pass #14)

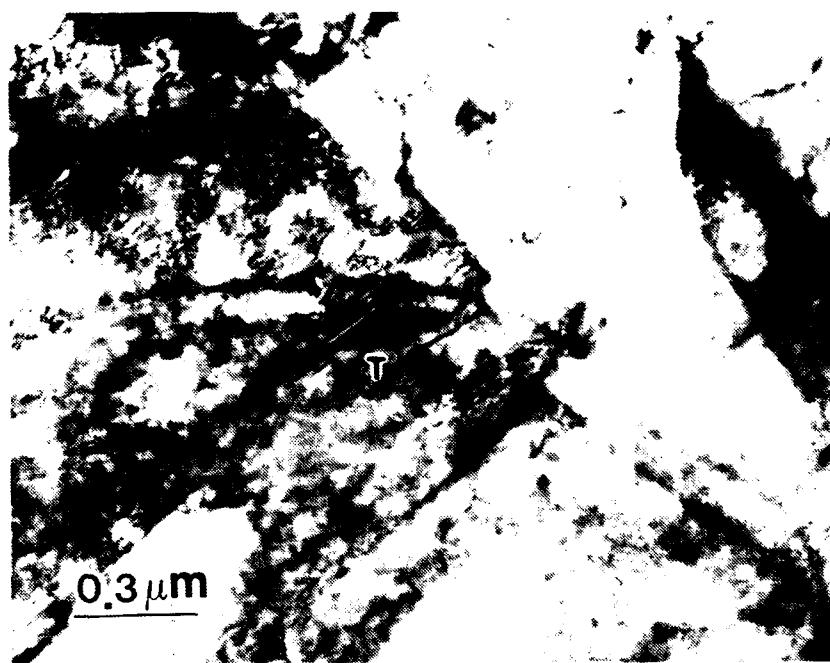


Figure 37. TEM Micrograph of Sample W2 (Pass #14)

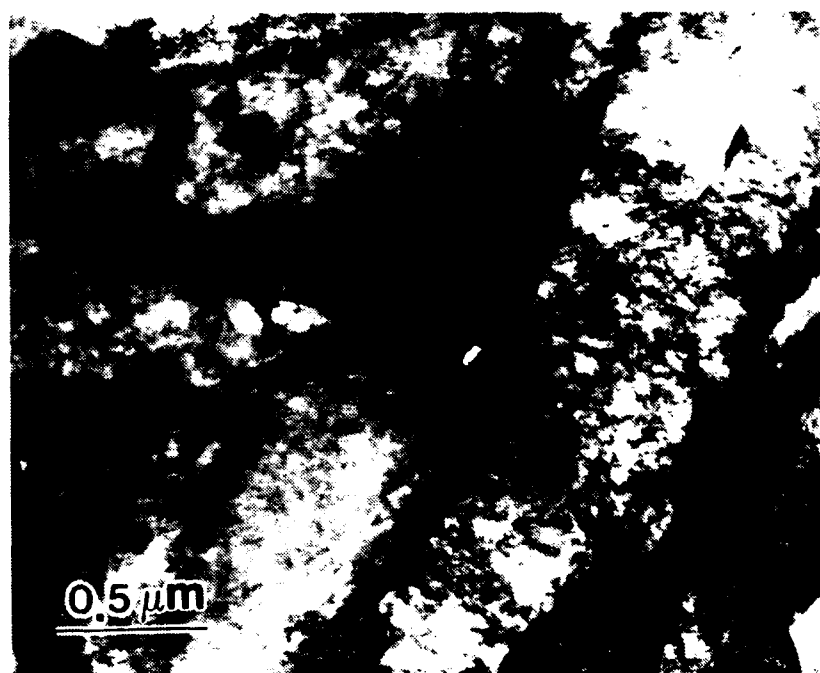


Figure 38. TEM Micrograph of Sample W2 (Pass #14)



Figure 39. TEM Micrograph of Sample W2 (Pass #14)

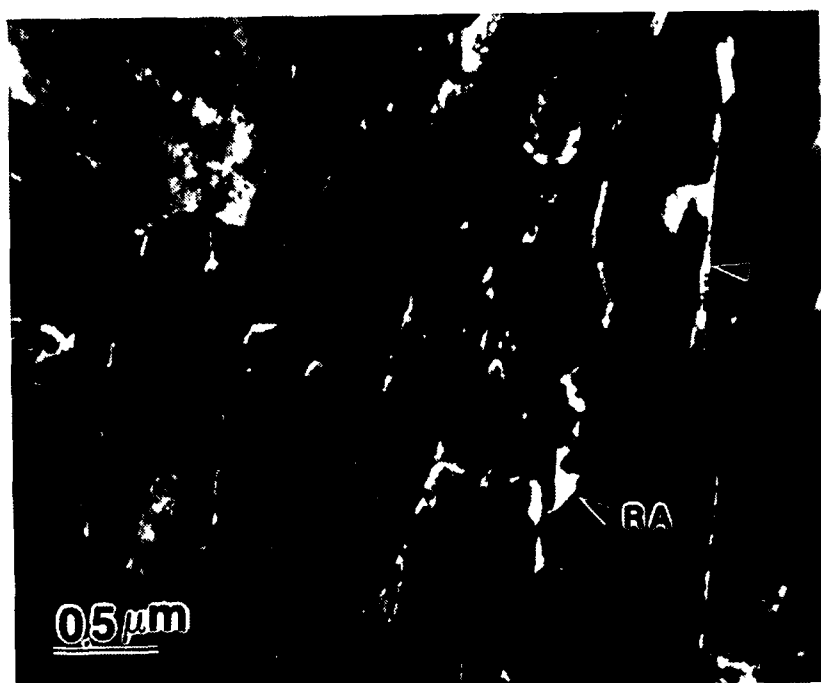


Figure 40. Dark Field TEM Micrograph of Figure 39

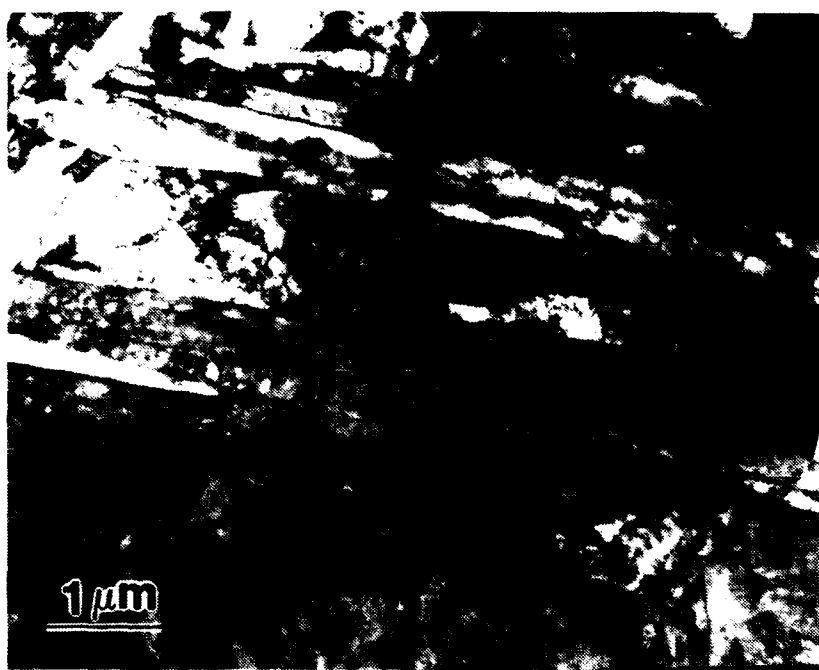


Figure 41. TEM Micrograph of Sample W6

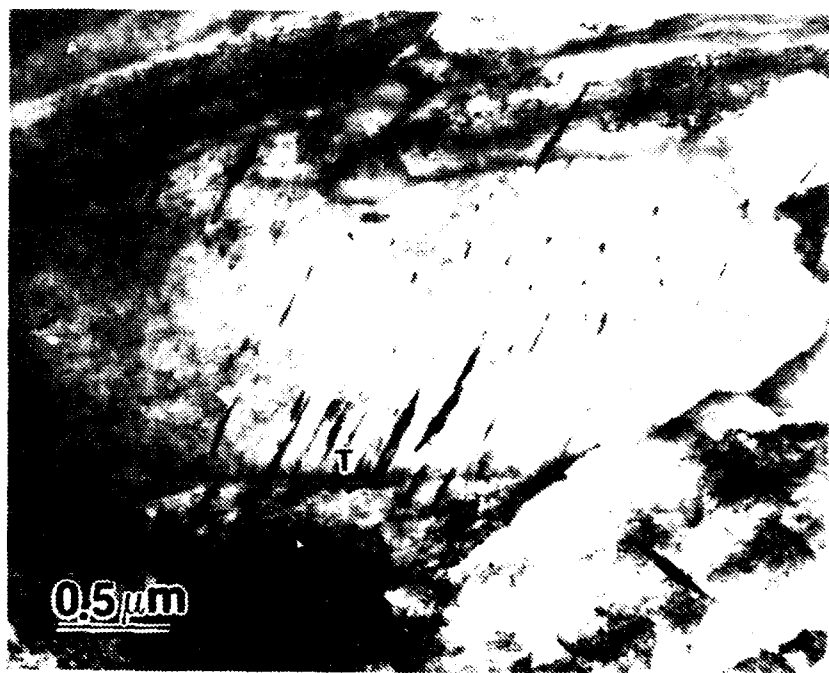


Figure 42. TEM Micrograph of Sample W6

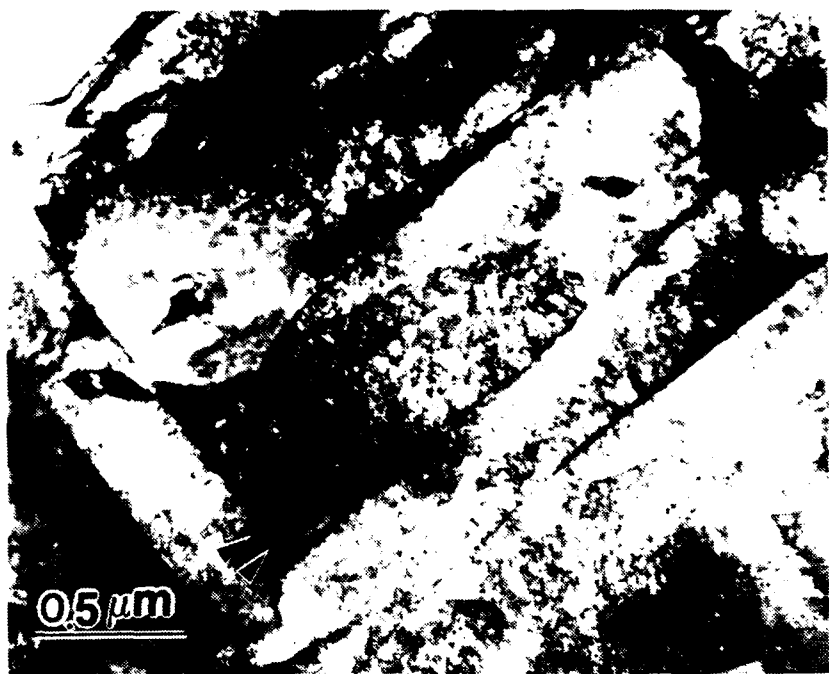


Figure 43. TEM Micrograph of Sample W6

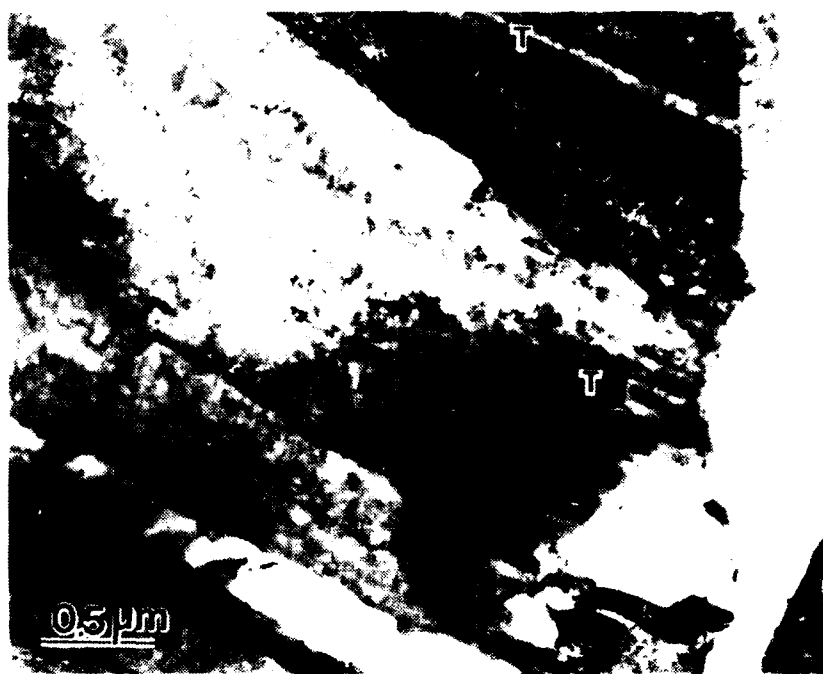


Figure 44. TEM Micrograph of Sample W6

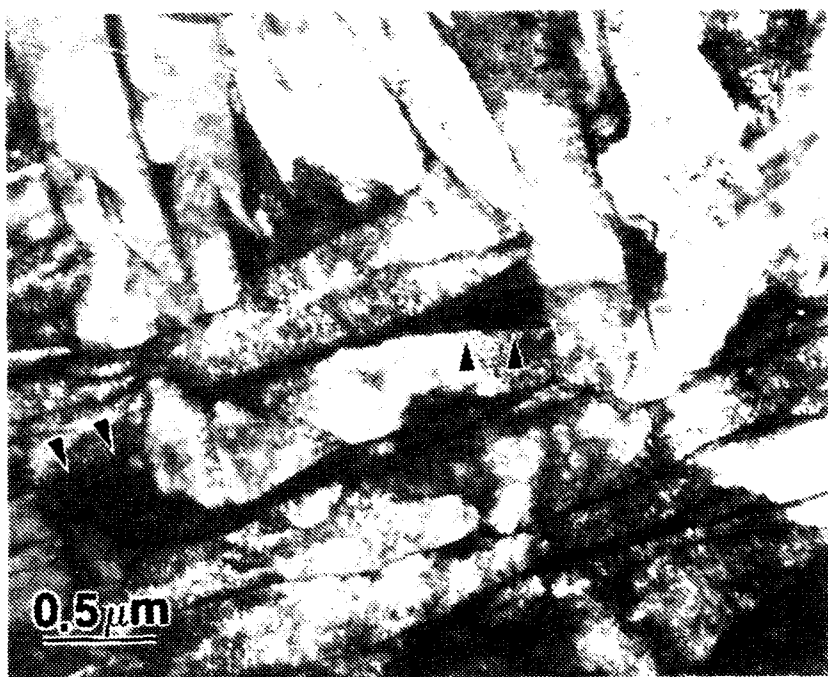


Figure 45. TEM Micrograph of Sample W58



Figure 46. TEM Micrograph of Sample W58



Figure 47. TEM Micrograph of Sample W58

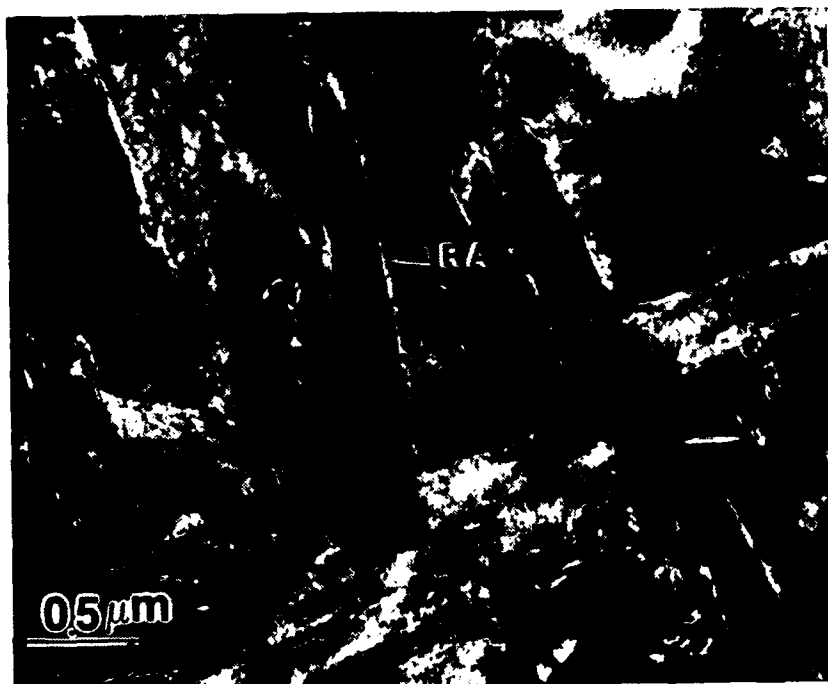


Figure 48. Dark Field TEM Micrograph of Figure 47

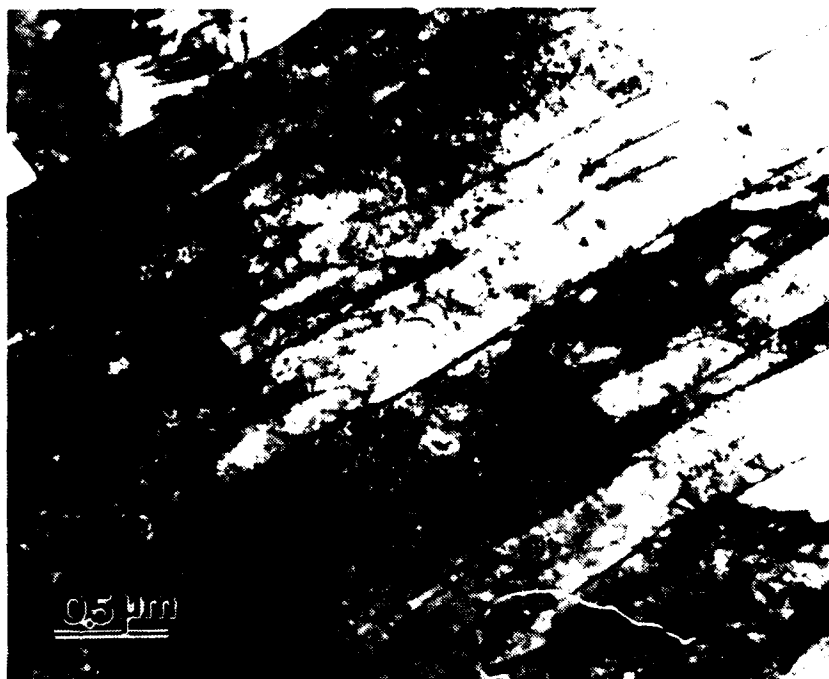


Figure 49. TEM Micrograph of Sample W60



Figure 50. TEM Micrograph of Sample W60

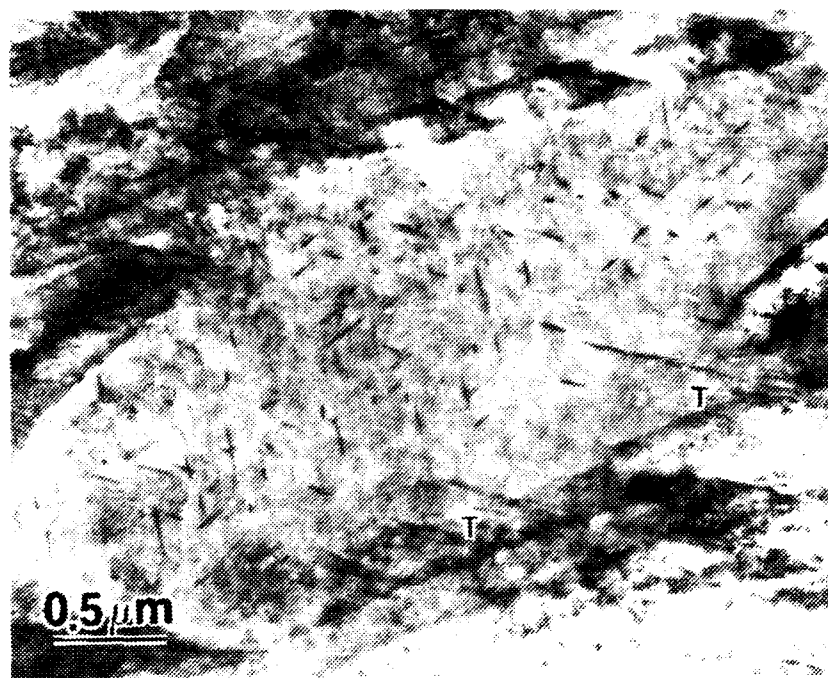


Figure 51. TEM Micrograph of Sample W60

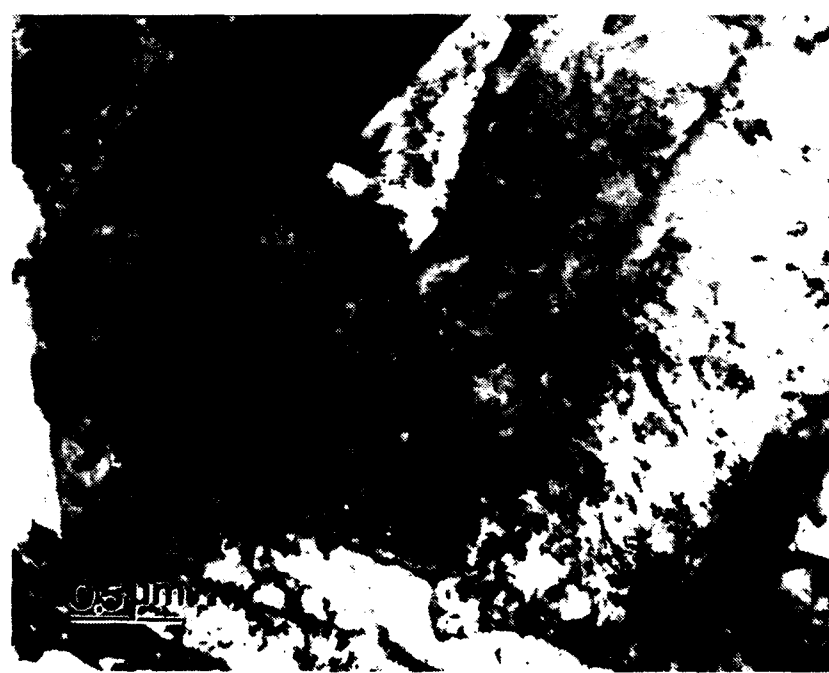


Figure 52. TEM Micrograph of Sample W60

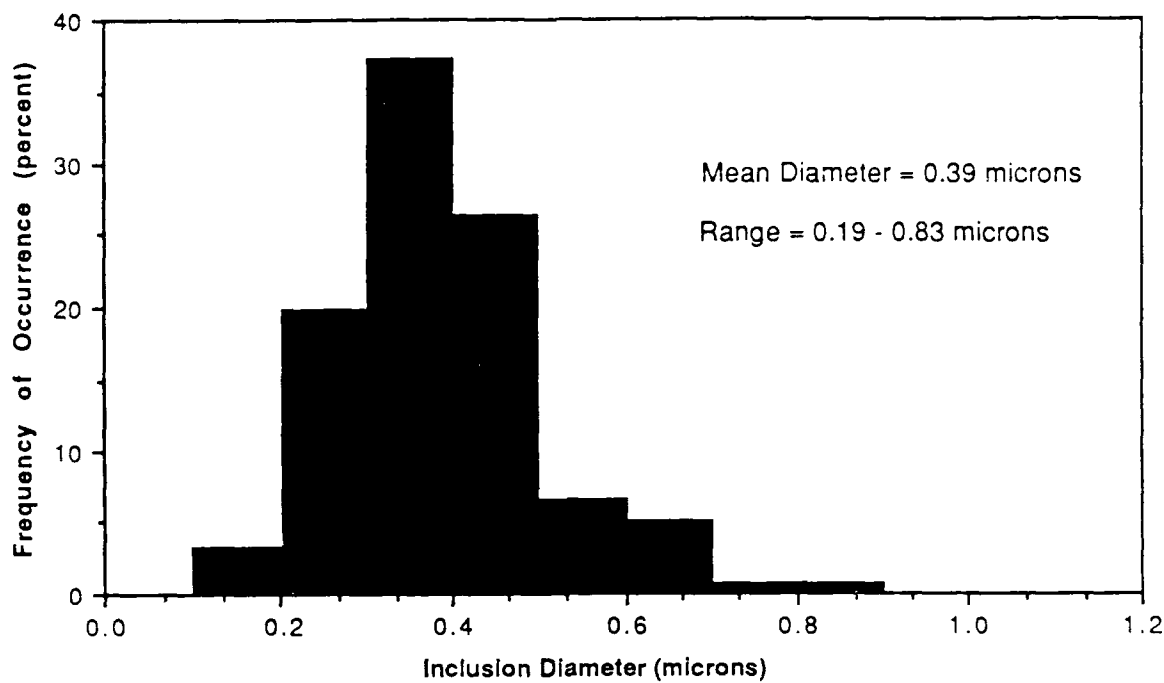


Figure 53. Inclusion Size for Sample W2

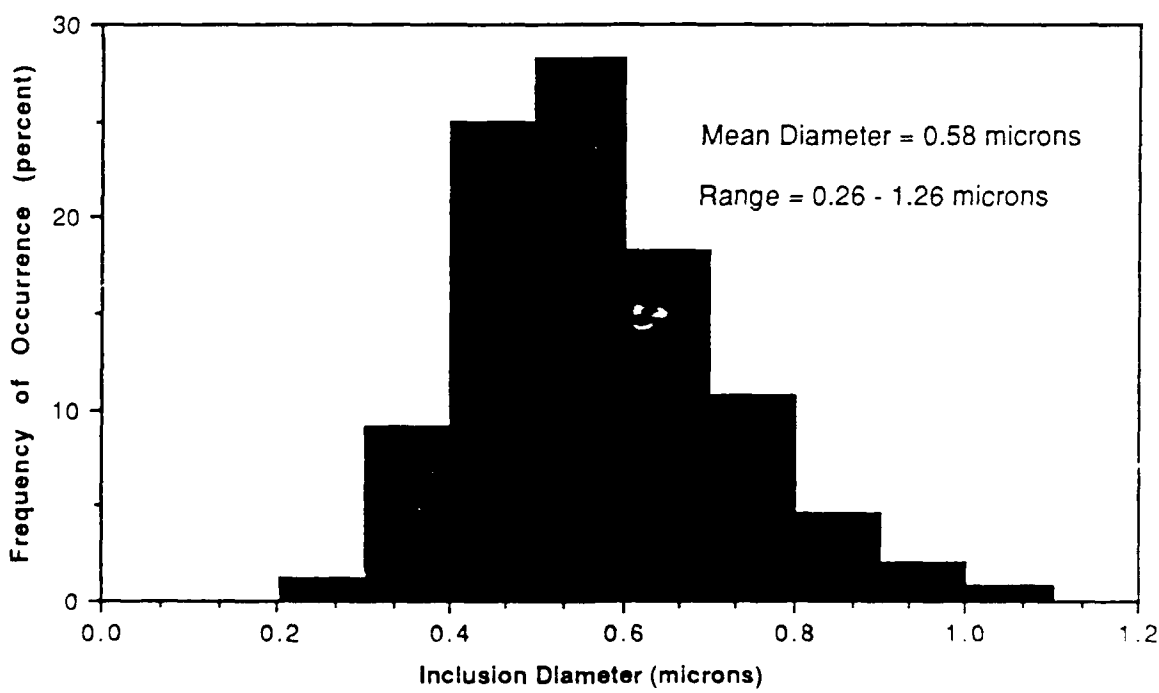


Figure 54. Inclusion Size for Sample W6

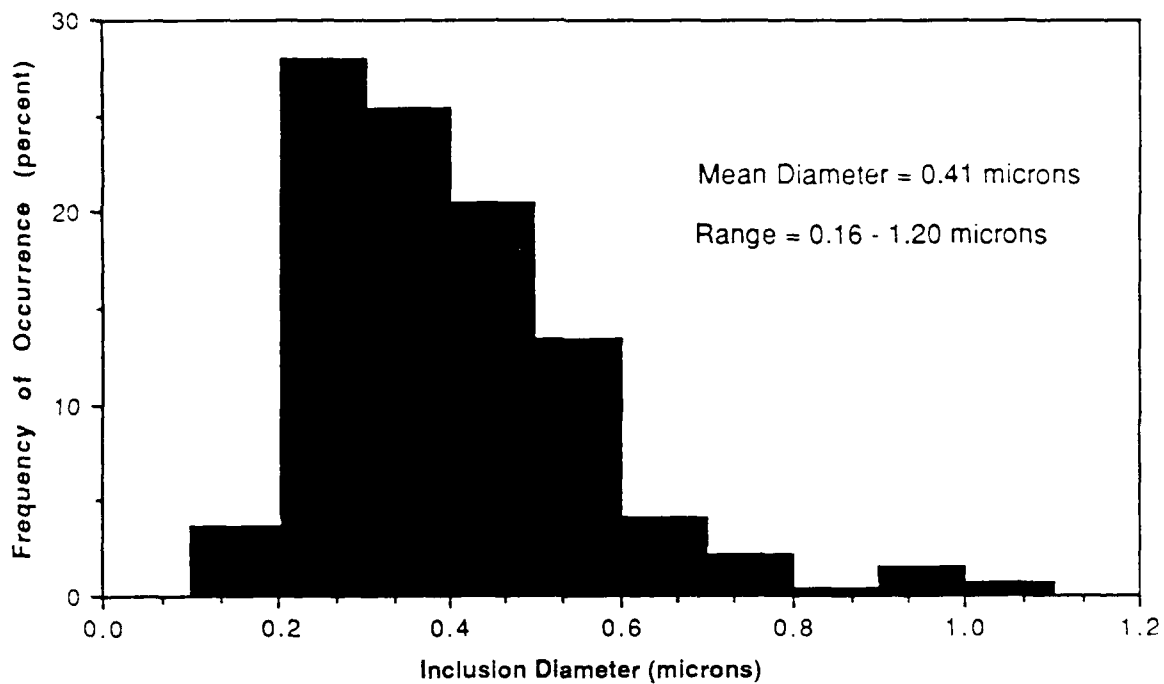


Figure 55. Inclusion Size for Sample W58

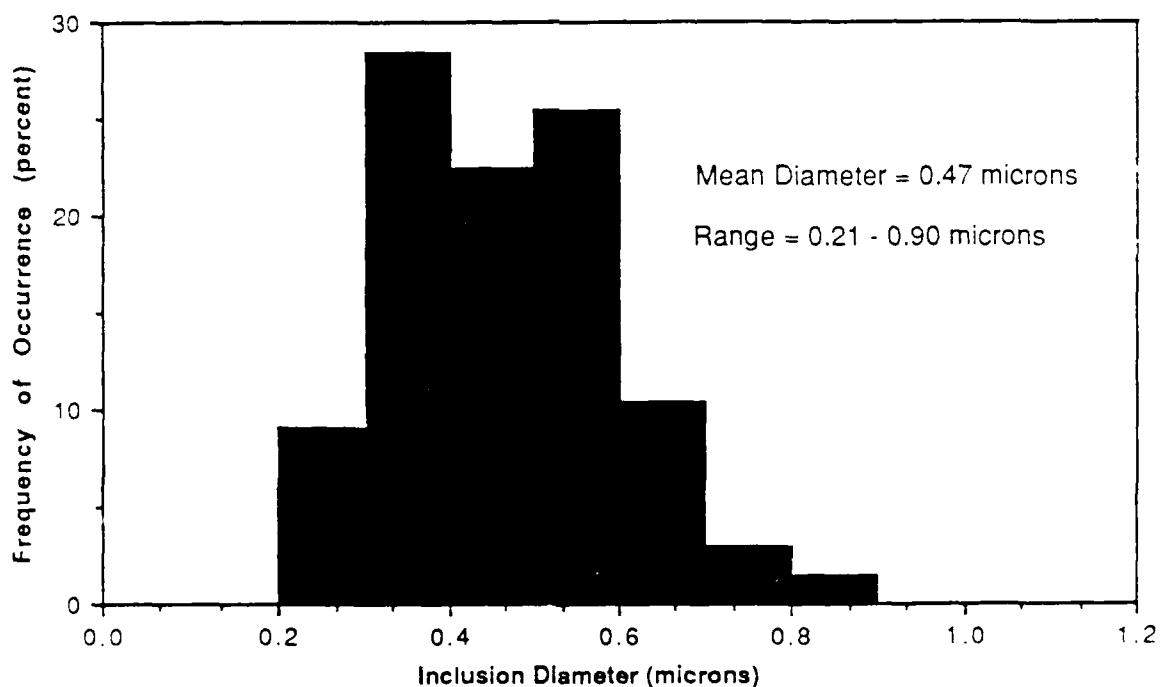


Figure 56. Inclusion Size for Sample W60

## LIST OF REFERENCES

1. U. S. Steel Applied Research Lab Report 40.18-001, The Effect of Heat Treatment on the Strength and Toughness of Promising 130 to 150 ksi Yield Strength Submarine Hull Steels, by D. S. Dabkowski, S. J. Mangello, and L. F. Porter, pp. 2-40, March 1963.
2. Challenger, K. D., Brucker, R. B., Elger, W. M., and Sorek, M. J., "Microstructure-Thermal History Correlations for HY-130 Thick Section Weldments," Welding Journal, Research Supplement, pp. 254s-261s, August 1984.
3. Electric Boat Division, General Dynamics, Task 3.23, N--24-80-C-2021, Potential Weight and Cost Effects of Using HY-130 Steel in Submarine Nonpressure Hull Structures, by R. Pepin, February 1985.
4. David Taylor Naval Ship Research and Development Center Report SME-85/109, Welding of Thin Section HY-130 Steel Progress Report, by R. J. Wong, pp. 1-38, January 1986.
5. Easterling, K., Introduction to the Physical Metallurgy of Welding, Butterworths, pp. 80-103, 1983.
6. Glover, A. G., McGrath, J. T., Tinkler, M. J., and Weatherly, G. C., "The Influence of Cooling Rate and Composition on Weld Metal Microstructures in a C/Mn and a HSLA Steel," Welding Journal, Research Supplement, pp. 267s-273s, 1976.
7. Askeland, R. A., The Science and Engineering of Materials, PWS Publishers, pp. 300-364, 1984.
8. Thomas, G., "Retained Austenite and Tempered Martensite Embrittlement," Metallurgical Transactions, Volume 9A, pp. 439-450, March 1978.
9. Biss, V., and Cryderman, R. L., "Martensite and Retained Austenite in Hot-Rolled, Low-Carbon Bainitic Steels," Metallurgical Transactions, Volume 2, pp. 2267-2276, August 1971.
10. Farrar, R. A., and Harrison, P. L., "Acicular Ferrite in Carbon-Manganese Weld Metals an Overview," Journal of Materials Science 22, pp. 3812-3820, April 1987.

11. Ricks, R. A., Howell, P. R., and Barrite, G. S., "The Nature of Acicular Ferrite in HSLA Steel Weld Metals," Journal of Materials Science 17, pp. 732-740, 1982
12. Grong, O., and Matlock, D. K., "Microstructural Development in Mild and Low-Alloy Steel Weld Metals," International Metals Reviews, Volume 31, Number 1, pp. 27-46, 1986.
13. Abson, D. J., and Dolby, R. E., "Microstructural Transformations in Steel Weld Metals - a Reappraisal," Welding Institute Research Bulletin, pp. 202-206, July 1978.
14. Lancaster, J. F., Metallurgy of Welding, Allen & Unwin Publishers Ltd., pp. 148-149, 1987.
15. Byrne, J. P., Palko, W. A., and Zanis, C. A., "Processing of HY-130 Steel Castings," American Foundrymen's Society Transactions, Volume 84, pp. 193-202, 1976.
16. Chen, C., Thompson, A. W., and Bernstein, I. M., "The Correlation of Microstructure and Stress Corrosion Fracture of HY-130 Steel Weldments," Metallurgical Transactions, Volume 11A, pp. 1723-1730, October 1980.
17. Connor, L. P., Rathbone, A. M., and Gross, J. H., "Development of Procedures for Welding HY-130(T) Steel," Welding Journal, Research Supplement, Volume 46(7), pp. 309s-321s, 1967.
18. Sarikaya, M., Steinberg, B. G., and Thomas, G., "Optimization of Fe/Cr/C E-be Structural Steels for Improved Strength and Toughness," Metallurgical Transactions, Volume 13A, pp. 2227-2237, December 1982.
19. Speich, G. R., and Leslie, W. C., "Tempering of Steel," Metallurgical Transactions, Volume 3, pp. 1043-1054, May 1972.
20. Ritchie, R. O., Castro Cedeno, M. H., Zackay, V. F., and Parker, E. R., "Effects of Silicon Additions and Retained Austenite on Stress Corrosion Cracking in Ultrahigh Strength Steels," Metallurgical Transactions, Volume 9A, pp. 35-40, 1978.
21. Kim, Y. H., Kim, H. J., and Morris, J. W., Jr., "The Influence of Precipitated Austenite on Hydrogen Embrittlement in 5.5 Ni Steel," Metallurgical Transactions, Volume 17A, pp. 1157-1162, July 1986.

22. Deb, P., Challenger, K. D., and Therrien, A. E., "Structure-Property Correlation of Submerged-Arc and Gas-Metal-Arc Weldments in HY-100 Steel," Metallurgical Transactions, Volume 18A, pp. 987-998, June 1987.
23. Enis, Y. A., and Telford, R. T., "Gas Metal-Arc Welding of HY-130(T) Steel," Welding Journal, Research Supplement, pp. 271s-278s, June 1968.
24. ASTM Special Technical Publication 494, Welding the HY Steels, by R. W. Flax, R. E. Keith, and M. D. Randall, pp. 12-24, April 1971.
25. Bhatti, A. R., Saggese, M. E., Hawkins, D. N., Whiteman, J. A., and Golding, M. S., "Analysis of Inclusions in Submerged Arc Welds in Microalloyed Steels," Welding Journal, Volume 63(7), pp. 224s-230s, July 1984.
26. Andrews, K. W., "Empirical Formulae for the Calculation of Some Transformation Temperatures," Journal of the Iron and Steel Institute, pp. 721-727, July 1965.
27. Vander Voort, G. F., Metallography - Principles and Practices, McGraw-Hill Book Company, p. 534, 1984.

## INITIAL DISTRIBUTION LIST

1. Defense Technical Information Center 2  
Cameron Station  
Alexandria, Virginia 22304-6145
2. Library, Code 0142 2  
Naval Postgraduate School  
Monterey, California 93943-5002
3. Department Chairman, Code 69Hy 1  
Department of Mechanical Engineering  
Naval Postgraduate School  
Monterey, California 93943-5000
4. Dr. S. Saboury 2  
P.O. Box 51922  
Pacific Grove, California 93950
5. Dr. J. M. B. Losz, Code 69Lo 2  
Department of Mechanical Engineering  
Naval Postgraduate School  
Monterey, California 93943-5000
6. Professor T. R. McNelley, Code 69Mc 1  
Department of Mechanical Engineering  
Naval Postgraduate School  
Monterey, California 93943-5000
7. Mr. Paul W. Holsberg, Code 2815 1  
David Taylor Naval Ship Research  
and Development Center  
Annapolis, Maryland 21402-5067
8. Mr. R. J. Wong, Code 2821 1  
David Taylor Naval Ship Research  
and Development Center  
Annapolis, Maryland 21402-5067
9. LT Dean M. Pedersen 2  
Assistant Aegis Test Director for DDG-51  
Operational Test and Evaluation Force  
Norfolk, Virginia 23511-6388
10. LT M. H. Heinze, USN, Code N64 1  
Commander Naval Surface Force, U. S. Pacific Fleet  
NAB Coronado  
San Diego, California 92155-5035